Title: **Evolution of the growth plate into a spatially separated structure allows bone growth on land.**

Authors: Meng Xie[1], Pavel Gol'din[2], Anna Nele Herdina[1,19], Jordi Estefa[3], Ekaterina V Medvedeva[4], Lei Li[1], Phillip T Newton[1,5], Svetlana Kotova[4,6], Boris Shavkuta[4,7], Aditya Saxena[8], Lauren T Shumate[9], Brian Metscher[10], Karl Großschmidt[11], Shigeki Nishimori[9], Anastasia Akovantseva[4,7], Irene Linares Arregui[12], Paul Tafforeau[13], Kaj Fried[14], Mattias Carlström[1], Andras Simon[15], Christian Gasser[12], Henry M Kronenberg[9], Murat Bastepe[9], Kimberly L. Cooper[8], Peter Timashev[4,6,7], Sophie Sanchez[3,13,16], Igor Adameyko[1,17], Anders Eriksson[18], Andrei S Chagin[1,4*]

Affiliations

1. Department of Physiology and Pharmacology, Karolinska Institutet, Stockholm, Sweden
2. Department of Evolutionary Morphology, Schmalhausen Institute of Zoology of NAS of Ukraine, Ukraine
3. Science for Life Laboratory and Uppsala University, Subdepartment of Evolution and Development, Department of Organismal Biology, Uppsala, Sweden
4. Institute for Regenerative Medicine, Sechenov University, Russia
5. Department of Women's and Children's Health, Astrid Lindgren Children's Hospital, Karolinska University Hospital, Sweden
6. Semenov Institute of Chemical Physics, Russia
7. Institute of Photonic Technologies, Research center "Crystallography and Photonics", Russia
8. Division of Biological Sciences, University of California San Diego, USA
9. Endocrine Unit, Department of Medicine, Massachusetts General Hospital and Harvard Medical School, Boston, U.S.A.
10. Department of Theoretical Biology, University of Vienna, Austria
11. Bone and Biomaterials Research, Center for Anatomy and Cell Biology, Medical University of Vienna, Vienna, Austria
12. Department of Solid Mechanics, KTH Royal Institute of Technology, Stockholm, Sweden
13. European Synchrotron Radiation Facility, Grenoble Cedex, France
14. Department of Neuroscience, Karolinska Institutet, Stockholm, Sweden
15. Department of Cell and Molecular Biology, Centre of Developmental Biology for Regenerative Medicine, Karolinska Institute, Stockholm, Sweden
16. Sorbonne Université – CR2P – MNHN, CNRS, UPMC, Paris, France
17. Department of Molecular Neurosciences, Medical University of Vienna, Austria
18. Department of Mechanics, KTH Royal Institute of Technology, Stockholm, Sweden
19. Division of Anatomy, MIC, Medical University of Vienna, Austria

*Corresponding author:
Andrei S Chagin andrei.chagin@ki.se

Abstract

Growth plates are narrow discs of cartilage, ultimately required for longitudinal growth of all mammals including humans. However, originally the growth plate and articular cartilage were a single anatomical entity, an epiphyseal cartilage, as appeared in early tetrapods and in mammalian development. The reason, why the growth plates evolved as spatially separate organs, remains unknown.

Here, we demonstrate that the epiphyseal growth plate first appeared as an individual organ in amniotes due to the formation of a novel bony structure, the secondary ossification center (SOC), which spatially separates articular cartilage and the growth plate. Since amniotes translocate their entire growth period on land, we next explored the role of mechanical demands faced by bones growing under weight-bearing conditions. Comparison of mammals whose limbs are subjected to greater or lesser mechanical demands (i.e., Chiropterans (bats), Cetaceans (whales) and Dipodidae (jerboa)) revealed that the presence of an SOC is correlated to the extent of these demands. Mathematical modelling in combination with physical and biological experiments showed that the SOC reduces shear and normal stresses within the growth plate, allowing epiphyseal chondrocytes to withstand a six-fold higher load before undergoing caspase-dependent apoptosis via the YAP-p73 pathway. Furthermore, the hypertrophic chondrocytes, the cells primarily responsible for bone elongation were least mechanically stiff and most sensitive to weight bearing.

Our results demonstrate that evolution of the epiphyseal cartilage into a separate organ allows epiphyseal chondrocytes to withstand the high mechanical stress placed on them by the terrestrial environment.

Main text

The skeleton articulates via articular cartilage and grow in length via the epiphyseal cartilage, often presented as growth plates, tiny discs of cartilage located to the end of long bones and containing epiphyseal chondrocytes. These chondrocytes proliferate, align in the longitudinal direction and then undergo several-fold of enlargement (hypertrophy). Thereafter hypertrophic chondrocytes undergo apoptosis or trans-differentiation[1] leaving their calcified extracellular matrix as a scaffold for invading blood vessels and osteoblasts to form new bone tissue. The process of bone growth on cartilage template is called endochondral bone formation. Recent 3D microanatomical characterization of the 380-million-year-old lobe-finned fish *Eusthenopteron*[2] revealed longitudinally-oriented trabeculae within the shaft of their humeri (Fig. 1, A). This strongly indicates that endochondral ossification facilitated bone elongation in stem tetrapods in a similar manner to present-day mammals (Fig. 1, A to C)[2,3].

In humans as well as in the most common experimental models employed to study bone growth (i.e., mice, rats and rabbits) the growth plate is separated from the articular cartilage by a bony fragment called bony epiphysis in

anatomical/orthopedic terminology and the secondary ossification center (SOC) in developmental terminology. In mice, rats and humans this skeletal element forms during early postnatal development and splits the initially contiguous cartilaginous element (called cartilaginous epiphysis) into two independent structures, the growth plate and articular cartilage (Fig. S1, A and B)[4].

Interestingly, this spatial separation of cartilaginous epiphysis is not always required for articulation or bone growth, since it is absent in several vertebrate taxa, such as Stem tetrapods [2,3], Chelonians, Crocodilians and Urodeles[5,6] (see example of salamander cartilage in Fig. S1, C and D).

The above observations pose an intriguing question about the primary reasons behind evolution of cartilaginous epiphysis into two functionally and spatially separated structures, one responsible for articulation of the skeleton and another for its growth. Since both structures are involved in numerous clinical issues (i.e., growth failure in children, osteoarthritis in seniors), the understanding of the underlying reasons behind appearance of these structures seems to be of clinical importance.

It worth mentioning that Haines in 1942 compared the anatomy of epiphyses among different tetrapods and proposed that such a separation would evolve to improve mechanical properties of the cartilaginous joint[7]. An alternative hypothesis (based on mathematical modeling) suggested that the appearance of the SOC would not be a cause of mechanical changes, but a result of it[8]. Here, we performed evolutionary analysis, a series of different zoological comparisons, mathematic modelling, physical tests and biological experiments to address this important question.

Evolutionary analysis revealed that SOCs appeared in the long bones of amniotes and are present in all synapsids (including mammals) (Fig. 1, D). Some stem mammals may have evolved a SOC [i.e., *Niassodon*[9] (Fig. 1, D)], but most of them have not[10,11]. Sauropsids exhibit a great diversification of bone ossification: SOCs form in squamates (lizards) and calcified secondary centers (SCs) forms in sphenodontids (Fig. 1, D), whereas Chelonians (turtles and tortoises) and crocodilians do not possess an SOC[6]. Instead, marrow protrudes unevenly into epiphyseal cartilages leaving hypertrophic chondrocytes in between those protrusions while forming trabecular bones on their sides[6]. Bird's long-bones can form a SOC (e.g., proximal epiphysis of the tibiotarsus in the sparrow, Fig. S2), but mostly ossify their long bones without forming a SOC[12]. In both cases, trabecular protrusions further extend towards the epiphysis[6,7], in a manner, which is in principle resembling marrow protrusions in crocodilians and chelonians. The bones of non-avian dinosaurs appear to have been organized in a manner similar to birds (i.e., extended protrusions[10,11]) while SOCs have not been reported in these groups to the best of our knowledge. The absence of SOCs in anamniotes and its appearance in different orders in amniotes indicates evolutionary convergences and suggests that SOCs might have played an important and previously unexplored adaptive role for the appendicular skeleton functioning.

Anamniotes spend their juvenile growth period in an aquatic environment with amniotes being the first to shift their entire lifecycle on land. Such habitat change poses an engineering challenge to the skeleton, which must be rigid

enough to bear the body weight during wide-ranging joint movements and yet flexible enough to allow bone growth. Accordingly, we reasoned that appearance of the SOC might help meeting this challenge.

To test an association between the SOC and mechanical demands, we first examined the skeletal development of Chiroptera (bats), who use their extremities in a highly specialized manner. The newborn pups must cling to their mother or to the roost during their mothers' flights for foraging or relocation. We expect that the feet and thumbs (1st finger) of the wing encounter a greater weight bearing demand than the long wing bones that start to be utilized after about 2-3 weeks of age[13-16]. Accordingly, we analyzed the feet and thumb ossification compared to the rest of the wing bones.

We found that in newborn bat pups' development of the SOCs in the hindlimbs and thumbs is much more advanced than in the wings (Fig. 1, E and Video S1), which is in line with the heavy mechanical demands posed on these particular skeletal elements at birth. This difference was particularly pronounced in autopods with the feet and the thumb heavily ossified, whereas other bones of the wing have no SOC at all (Fig. 1, F to G). This differential pattern of ossification was apparent during ontogenesis and was general for the Chiroptera order (Fig. 1, H and I, summary of 6 species where ontogeny data were available to us) and primary data for all 13 analyzed species are presented (Supplementary data file 1). Chiroptera species differ widely in their foraging and roosting ecology, behavior of juvenile bats, litter size, and lifespan[17-21], which likely resulted in some variation among species.

Interestingly, the SOCs in the feet and the thumbs of some species of bats are well-developed even before birth (Supplementary data file 1) and the pups of certain species (*Mops condylurus*, *Artibeus jamaicensis*, *Megaloglossus woermani* and *Rousettus celebensis*) are born with feet nearly in adult size[17,19] (see also Fig. 1F for *A. jamaicensis*). In contrast, the wings (except thumb) start to be used much later as compared with the feet and, accordingly, a SOC develops in wing bones at the late juvenile stage. Thus, there is a clear association between mechanical demands and the time of the SOC appearance. Interestingly to note that appearance of the SOC in the embryonic feet and thumb suggests that a genetic program governing SOC development precedes the mechanical influence.

To further verify the association between the level of ossification and mechanical demands in an unrelated order we analyzed SOC development in a bipedal three-toed jerboa (*Jaculus jaculus*) of the family of Dipodoidea rodents. By monitoring the acquisition of bipedality in the jerboa we found that they employ only front limbs for crawling during the first 2 weeks of age, start using hind limbs (becomes quadrupedal) at 3 weeks of age and become fully bipedal at 4 weeks of age[22] (Video S3). Consistent with the mechanical use, formation of the SOC in the front limbs significantly preceded its formation in the hind limbs (Fig. 1K, L, and Fig. S3). It is interesting to point out that development of the SOC also coincides with the changes in gait pattern from crawling to walking in mice and rats (Fig. S1, A and B).

Following the same logic, we reasoned that the evolution of aquatic mammals from land to water, such as the cetaceans (whales) with a streamlined body and flippers (Fig. S4, A), might have led to the loss of this specialized structure. In early

cetaceans from Eocene era (56-33.9 Mya), the epiphyseal plates of the forelimbs are structurally similar to those of terrestrial mammals, as evident for *Maiacetus inuus*[23] and *Dorudon atrox*[24] (Fig. S4, B1 and B2, respectively). However, in extant baleen whales of Balaenopteridae family the SOCs in metacarpals and phalanges are extremely small but still well-developed in the distal radius and ulna (Fig. S4, B3). Balaenidae family, another extant lineage of baleen whales, demonstrates the most advanced limb transformation, with extreme reduction in SOC size in the distal radius, ulna and metacarpals; unusually small or even missing carpal elements; and a fibrocartilaginous structure between the zeugopodium and metacarpals (Fig. S4, B4).

Toothed whales from the Miocene era to the present demonstrate more diverse secondary ossification. Iniidae (Amazon River dolphins) do not have distinct epiphyseal plates, but rather multiple small SOCs (Fig. S4, B6). SOCs are formed in both Platanistidae and certain Delphinoidea (Fig. S4, B5), whereas in Ziphiidae and the narwhal *Monodon monoceros* (Delphinapteridae), SOCs are reduced in size (Fig. S4, B7). In another member of Delphinapteridae, the beluga whale *Delphinapterus leucas* X-ray examination revealed only the remnants of SOC in metacarpals and phalanges (Fig. S4, D). Finally, the most advanced epiphyseal transformation is seen in the killer whale *Orcinus orca* (Delphinidae) (Fig. S4, B8) and sperm whale *Physeter catodon*[25,26] (Fig. S4, B10), in which the SOCs of the distal radius, ulna and metacarpals are extremely reduced in size (and even absent) and a fibrocartilaginous structure is formed in the carpal area (Fig. S4, B8,10). CT scan revealed complete lack of the SOC in *Orcinus orca* (Fig. 1, J and Video S2), which was further confirmed by radiograph (Fig. S4, C). Thus, the return of cetaceans to the aquatic environment was associated with a reduction in the size of SOCs, including their complete loss in some species.

These evolutionary and comparative observations in unrelated animals suggest that evolving of the SOC is associated with the mechanical demands imposed onto the skeletal elements. However, alternative explanations, such as temporal differences in growth plate maturity, cannot be fully excluded in these associative studies. We therefore set up a series of modelling and functional experiments to seek further support for our mechanical demand hypothesis.

To explore the potential effects of SOC on stress distribution within the epiphyseal cartilage associated with the mechanical impact, we employed finite element analysis (FEA) based on a modification of the model developed by Carter and co-workers[8,27] (Fig. 2, A, see the method section for modelling details). For modelling of local forces, octahedral shear stress was considered to be the most significant stress on chondrocytes[8]. FEA revealed that the presence of a SOC reduced the extent to which octahedral shear stress (associated with either a vertical or an angled load, the latter mimicking locomotion) was distributed to the region of the epiphyseal plate (Fig. 2, A), even with a supra-physiological load (Fig. S5, A).

Our FEA model also predicted that a SOC significantly enhanced the stiffness of the entire epiphyseal structure (note the tissue deflection in Fig. 2, A and Fig. S5, A), thereby preventing severe distortion and consequent instability of this structure during locomotion. To test this experimentally, we employed tibia bones from 10-day-old rats and 30-day-old mice, which at these time-points are comparable in size,

shape as well as mechanical properties of cartilage (Fig. S5, B and C), except that the rat tibia has not yet developed a SOC (called SOC- model), whereas mice tibia do have a well-developed SOC at this age (SOC+ model) (Fig. S1, A and B). To test FEA predictions we applied various dynamic loads to the SOC± bones. As predicted, the SOC improved the stiffness of these bones in connection with both vertical and angled loads (Fig. 2, B and C and Fig. S5, D to I). Although confounding variables cannot be fully excluded in this SOC± modelling system even despite comparable size, shape and mechanical properties of the bones, concurrence of mathematical predictions and physical tests further validate the model.

Thus, the SOC provides additional stiffness, while simultaneously reducing octahedral shear stress in the epiphyseal growth plate. Why might such protection be important at the cellular level? To address this question, we placed bones exposed to different loads into culture conditions for 48 hours to allowed cellular responses to load to manifest using previously optimized culture conditions[28]. Growth plate chondrocytes appeared to be highly sensitive to load, 40% died upon application of a 1N load as revealed by propidium iodide (PI) staining, whereas the SOC clearly protected these cells, allowing them to withstand a load an order of magnitude higher (Fig. 2, F and G and Fig. S6). The unfavorable effect of loading was confirmed by the reduction in the expression of chondrocyte markers, like parathyroid hormone related peptide (PTHrP), Indian hedgehog (Ihh) (Fig. 2, D and E) and Collagen type X (Col X) (Fig. S5, K and L).

Cells frequently undergo programmed cell death (i.e., apoptosis) under unfavorable conditions. To test the hypothesis that chondrocytes under excessive mechanical load die by apoptosis, we first performed TUNEL assay, which detects fragmented DNA, a hallmark of apoptotic nuclei. This assay revealed that growth plate chondrocytes in the bones that lacked a SOC were apoptotic in response to high loads (Fig. 2, H to J and see Fig. S5, J for baseline control). In addition, Caspase-3, a protease that executes apoptosis, was also activated upon loading (Fig. 2, K). To further explore the underlying mechanism, we checked the activity of the Yes-associated protein 1/Tafazzin (YAP/TAZ) signaling pathway, which is well-known to be involved in mechano-sensing[29] and can promote apoptosis via the tumor suppressor protein, p73[30]. The levels and nuclear translocation of both the YAP (Fig. S7, A and Fig. S9, K and L) and p73 proteins (Fig. S7, B) were enhanced by loading and the overlapping distribution of these two proteins further supported activation of this signaling pathway (Fig. S7, C). Taken together, the caspase-dependent apoptosis, probably via the YAP-p73 pathway, appears to be triggered in vulnerable epiphyseal chondrocytes in the absence of the protective effects of a SOC.

We noticed that cell death was distributed unevenly along the longitudinal axis with a higher level of cell death in the hypertrophic zone (Fig. 3, A to D and Fig. 2, J). The levels of active caspase-3, YAP and p73 were also increased in the hypertrophic zone as compared with the resting/proliferative zone (Fig. 3, E to H and Fig. S8, A to D). In bones without a SOC death of hypertrophic chondrocytes can be detected at a load of as low as 0.2N (Fig. 3, I), whereas in the presence of a SOC hypertrophic cell death was observed only from 3-5 N loading and upwards (Fig. 3, A to D). At this loading

range no effect on chondrocyte proliferation can be observed (Fig. S8, E and F), suggesting particular sensitivity of hypertrophic chondrocytes to loading. The protective effect of SOC was particularly strong to this cellular population, which withstands 25-fold greater load with a SOC (comparing 0.2 N to 5N).

Our observations of a highly efficient protection prompted us to modulate the SOC size in age matched individuals, a less sensitive but more physiological setting. We recently reported that SOC development depends on angiogenesis and can be delayed by a vascular endothelial growth factor (VEGF) receptor blocker, axitinib[31] only in a narrow window when treatment is initiated from P18, but not from P21 in transgenic mice[32]. Similar inhibition was observed in wild-type mice (Fig. 3, J). The mice with delayed SOC development had a clear increase in apoptosis of hypertrophic chondrocytes as compared to control (Fig. 3, K). Additionally, we have analyzed mice with limb-specific activation of the stimulatory G-protein α-subunit (Gsα) that exhibit delayed SOC formation (Prx-Cre:Gsα^{R201H})[33]. To block immediate elimination of dead hypertrophic chondrocytes by ingrowing blood vessels we inhibited angiogenesis in these mice and corresponding controls with axitinib at the time window, which does not interfere with SOC formation (P21-P29, Fig. 3, K), but allows delay elimination of hypertrophic chondrocytes[32]. Analysis of these mice confirmed decreased SOC size and revealed increased death of hypertrophic chondrocytes (Fig. S8, G and H). It has to be emphasized that in both pharmacological and genetic models mice actively run, exposing their growth plates to the weight-associated loads, but have decreased body mass (axitinib-treated mice were 56.6±11.2% of control and Prx-Cre:Gsα^{R201H} mice were 80±6.9% of control). Thus, the observed increase in cell death may be an underestimation of the level of cell death that would be expected in bones with an underdeveloped SOC under normal physiological weight.

Intriguingly, in our SOC± modeling system we also noticed that when loading was applied at an angle, dying hypertrophic chondrocytes were distributed unevenly, not only along the longitudinal axis (resting&proliferative - hypertrophic, Fig. 3), but also along the medial-lateral axis. Specifically, chondrocytes on the side opposite to the loading underwent more extensive apoptosis compared to the other side (Fig. 4, A to C). Similarly, the number of TUNEL-positive cells and the level of YAP were also the highest on the side opposite to the one where loading was applied (Fig. S9, C, E, G, I). Vertical loading did not affect the medial-lateral spatial distribution of cell death, thereby acting as a control (Fig. S9, A, B, D, F, H, J). Similarly, a medial-lateral distribution of cell death was observed in a mouse model where inhibition of the SOC was achieved by chondrocyte-specific ablation of the salt-induced kinase 3 (Sik3) (Col2-Cre:Sik3-FL/FL mice)[34]. In these actively running mice SOC development was substantially delayed (Fig. 4, D) and death of hypertrophic chondrocytes was increased in the lateral sides as compared with the middle part of the growth plate (Fig. 4, E).

This uneven distribution of cell death along the medial-lateral axis cannot be explained by the octahedral shear stress, since with angled loading this stress is the highest in the central region of the growth plate (Fig. 2, A). Our FEA model revealed that with angled loading, only the highest compressive principal stress (Fig. 4, F) and hydrostatic stress (Fig. S9, M and S10 for physiological and supra-physiological

loads, respectively) match the medial-lateral distribution of cell death observed above. Hydrostatic stress was not considered further, since it was also increased upon vertical loading in the model with a SOC, and therefore cannot be the target for the protection afforded by SOC (Fig. S9, M).

Thus, it appears that directional compressive stress is harmful to chondrocytes, especially to the hypertrophic chondrocytes. To understand this vulnerability to compressive stress we measured cell stiffness by applying atomic force microscopy (AFM) on live tissue sections as it has been shown that fixing or freezing the samples or isolating the cells might change their stiffness[35]. This approach revealed that hypertrophic chondrocytes were only a quarter as stiff as the columnar chondrocytes, from which they are derived (Fig. 4, G and H). Therefore, it is likely that the low stiffness of hypertrophic chondrocytes, in combination with their large size, render them particularly vulnerable to mechanical loading.

Long-bone elongation through endochondral bone formation has been conserved evolutionary since its development at least 400±20 Mya[2,3] and chondrocyte hypertrophy is a key aspect of this process, not only contributing to 59% (73% with the corresponding ECM) of growth[36,37], but also coupling cartilage resorption to the formation of new bone (e.g., via Ihh and VEGF secretion as well as matrix calcification)[38]. Thus, while juvenile growth in an aqueous environment makes no special demands on the mechanical properties of hypertrophic chondrocytes, transition on land poses the mechanical stress of weight bearing particularly on appendicular skeleton, which in turn might damage the hypertrophic chondrocytes precluding proper bone formation. Accordingly, it can be viewed that SOCs evolved to preserve the evolutionary ancient process of endochondral bone formation in specific terrestrial loading conditions.

However, numerous vertebrates lack SOCs. Among terrestrial crown amniotes the mammals and lepidosaurs have SOCs, whereas non-avian dinosaurs, crocodilians and chelonians lack this structure (Fig. 1, D). Instead, birds and dinosaurs (albeit we confirmed that some bones in some birds develop SOCs, Fig. S2) and, to a lesser extent, chelonian and crocodilians develop bone marrow protrusions with calcified or ossified walls that protrude deeply into the epiphyseal cartilage and sequester hypertrophic chondrocytes between them[7,12,39]. Modelling this system revealed that this design relieves the hypertrophic zone highly efficiently from loading-induced stress (Fig. S10). Chelonians and crocodilians have an epiphysis, which deviates the least from the most ancient types[7] and are likely execute partial protection of the hypertrophic chondrocytes by combining their metaphyseal longitudinal trabecular arrangement (Fig. S10) with partial reduction of the load-associated stress achieved by aquatic juvenile life style or crawling type of gait. These observations suggest that, despite employing different evolutionary strategies, amniotes appear to address the same issue of the poor compatibility of hypertrophic chondrocytes with the mechanical demands of terrestrial bone growth.

It is interesting to point out that SOC formation occurs at the expense of chondro-progenitors located in this area, which would theoretically limit the growth potential of all terrestrial animals. Expression of sonic hedgehog by SOC cells and

initiation of an epiphyseal stem cell niche by this bony structure[40] might be a secondary or parallel adaptation to overcome this loss of chondro-progenitors associated with SOC development.

In conclusion, our evolutionary observations, comparative zoology, paleontological analyses, mathematical modeling, physical tests as well as pharmacological and genetic interventions together strongly suggest that the primary reason behind appearance of a spatially defined growth plate is to shield the hypertrophic chondrocytes from mechanical stress associated with weight-bearing demands of bone growth in terrestrial environment. These observations can provide evolutionary, mechanistic and functional explanations for the Hueter-Volkmann law formulated during 1862-1897, which stating that "*increased mechanical compression reduces longitudinal bone growth while reduced mechanical loading increases it*"[41].

The understanding of the primary cause of spatially defined growth plate structure in mammals (including humans) might influence the design of sporting activities for young people during their most active period of growth and may also help develop new surgical strategies for the treatment of growth plate fractures.

Acknowledgements

This work was supported financially by EMBO Long-Term Fellowships (MX), and grants from the Swedish Research Council (ASC: 2016-02835; SS: 2015-04335), Karolinska Institutet (MX, ASC, LL, IA) including an SFO Stem/Regen junior grant (ASC), Bertil Hallsten Foundation (IA), EMBO Young Investigator Program (IA), Åke Wiberg Foundation (IA), Chinese Scholarship Council (LL), Stiftelsen Frimurare Barnhuset i Stockholm (PN, MX), Museum of the Southern Jutland (PG) and the internal start-up grant (5-top-100 program) from the Sechenov University to ASC. Experiments with atomic force microscopy and weight bearing animal models were financially covered by grants from Russian Science Foundation (#18-15-00401 to PT and #19-15-00241 to ASC).

O Lambert (IRSNB), MT Olsen (ZMUC), F Zachos (NMW), PHC Lina (Naturalis) and D Kalthoff (Museum of Natural History, Stockholm, Sweden) and J. Klembara (CU) provided access to the specimens in collection under their care. Synchrotron beamtime was allocated in response to a proposal accepted by the ESRF (EC203, SS; ES342, JE) and as in-house beam-time (PT). The authors thank F. Arnberg (Karolinska Institutet) and Astrid Haase (Medical University of Vienna) for the help with the micro-CT, CT and X-ray scans.

Materials and Methods

Ethics

Except for those involving AFM, all animal experiments were pre-approved by the Ethical Committee on Animal Experiments (Stockholm North Committee/ Norra Djurförsöksetiska Nämnden) or the Institutional Animal Care and Use Committee of the Massachusetts General Hospital and conducted in accordance with the provisions and guidelines for animal experimentation formulated by the Swedish Animal Agency.

Animal experiments involving AFM were pre-approved by the Ethics Committee of the Sechenov First State Moscow Medical University (Moscow, Russia).

Museum collections

The museum specimens of cetaceans were examined at the Royal Belgian Institute of Natural Sciences (Brussels, Belgium), Natural History Museum Stockholm (Stockholm, Sweden) and Zoological Museum, University of Copenhagen (Copenhagen, Denmark). The specimens shown in Fig. S4, B3 to 9 were preserved naturally, B1 to 2 are the casts of unprepared articulated skeletons and the carpal area in B10 is paraffinated (orange colour) so only ossifications on the surface can be seen. Please note that all Cetaceans analyzed where adult or sub-adult except one out of two sperm whales.

The museum specimens of Chiroptera were from the Naturalis Biodiversity Center (Leiden, Netherlands) and Natural History Museum Vienna (Vienna, Austria).

The humerus of *Eusthenopteron* (NRM P248d) comes from the Devonian locality of Miguasha (Quebec, Canada) and is housed in the collection of the Natural History Museum (Stockholm, Sweden). The humerus of *Seymouria* (MNG 7747) comes from the Permian locality of the Cutler Formation (Arroyo del Agua, North-Central New Mexico) and is housed in the collection of the Museum der Natur (Gotha, Germany). The humerus of the squirrel and the skeleton of the sparrow come from a private collection (PT).

Synchrotron scanning and 3D modeling

All these scans were performed at the beamline ID19 (European Synchrotron Radiation Facility, France) with a current of 200 mA or 16 bunch. Scanning and 3D-modeling of the humerus of *Eusthenopteron* were performed as described by [2]. The data were reconstructed using a single distance phase retrieval approach[42] based on a modified version of the algorithm of[43], applying an unsharp mask to the radiographs after the phase retrieval to enhance the trabecular mesh. The humerus of *Seymouria* was imaged with a voxel size of 3.48 µm using an optical system associated to a 47µm-thick GGG (i.e., a gadolinium gallium garnet crystal) scintillator and a FreLON 2k14 CCD detector[44]. The propagation distance was of 700 mm. The gap of the W150m wiggler was opened to 37 mm. The sample was imaged at 80 keV using a beam filtered with 0.25mm of tungsten and 2mm of aluminium. In half-acquisition conditions, 4998 projections were produced over 360° with a time of exposure of 0.15 s. Binned images (final 6.96µm voxel size) were reconstructed, segmented and 3D-modeled in the same manner as *Eusthenopteron*[2]. The scan of the humerus of *Sciurus vulgaris* was made with the same voxel size (3.48 µm) as for the humerus of *Seymouria* using the same optics (FreLON 2k14 CCD camera and a 47µm-thick GGG scintillator). The sample was imaged with a propagation distance of 500 mm. The beam was filtered with 0.14mm of tungsten, 0.14mm of copper and 2.8mm of aluminium. The gap of the W150m wiggler was opened to 50 mm, which resulted in an energy of 65.8keV. In half-acquisition conditions, 4998 projections were produced over 360° with a time of exposure of 0.15 s.

MicroCT and X-radiography

X-ray microtomography (microCT) imaging of *Pipistrellus pipistrellus* and other bats and X-radiography of *Delphinapterus leucas* were performed at the Department of Theoretical Biology, Faculty of Life Sciences, University of Vienna, Austria, and CT imaging of *Orcinus orca* was performed in the Karolinska Institutet (Stockholm, Sweden). The whole bat skeleton (Fig.1, E and Video S1) was imaged with a SkyScan 1174 (Bruker microCT; isotropic voxel size 21.7 μm, exposure 3.6 sec, averaging 4 frames, rotation step 0.39°, 360° scan, 50 kV, 8 W, tungsten x-ray source); and segmented in Amira 6.1. The wing and foot (Fig. 1, E1 and 2) were imaged with an Xradia MicroXCT (Zeiss X-Ray Microscopy; isotropic voxel size 8.8 μm (1) and 8.5 μm (2) respectively, exposure 20 sec, rotation step 0.3°, 180° scan, 80 kV, 8 W, tungsten x-ray source); and segmented in Amira (6.1). These specimens were mounted in 70% ethanol in tight-fitting tubes. The 3D surface renderings and measurements were produced in Amira (6.1).

Measurements and calculations of ossification level in Chiroptera

Bats are considered adult when both epiphyses of the metacarpo-phalangeal joint of the 4th finger have become fully ossified. The heights of the epiphyses and SOCs were obtained by microCT images (own data) using the Fiji software or from published images of limb bones (as specified in table S1). The height of the SOC was divided by the total height of the epiphysis (from joint to primary ossification center) and the ratio zero corresponds to non-ossified epiphysis and the value one to fully ossified epiphysis. In cases where the literature provided only gap values (non-visible area of soft tissue between two ossified elements), the total epiphyseal gap was divided 2/3 (metacarpus) to 1/3 (phalanx) to obtain an estimate of the total height of the epiphyses, while the height of the SOC was calculated by subtracting the proximal (metacarpal) or distal (phalanx) epiphyseal gap from the total height of the epiphysis.

For Fig. 1, the level of ossification of wing autopods was calculated as an average of the ossification of metacarpals 2-5 and proximal phalanges 2-5. Ossification of foot autopods was calculated as an average of the ossification of metacarpals 1-5 and proximal phalanges 1-5. Ossification of the thumb was calculated as an average of the metacarpal and proximal phalange. Ossification of the stylopod and zeugopod was calculated as an average of the humerus, radius, and ulna for wings femur, tibia, and fibula for legs. Proximal and distal epiphyses were combined for different skeletal elements whenever data for both sides are available.

Jerboa Housing and Movies

Jerboas were housed and cared for as previously described[45] and in accordance with UCSD institutional Animal Care and Use Committee guidelines. Individual jerboa pups from one litter were filmed at 7, 14, 21 and 28 days after birth in a well-lit room using an iPhone and without any flash lights to document locomotion.

Jerboa Skeletal Preparation

We followed a previously published skeletal preparation protocol[46] with minor modifications. All steps were performed on a rocker at room temperature. Freshly dissected and de-skinned samples were fixed in 100% ethanol for 24 hours. Samples were then treated with 100% acetone for 24hours. Fixed samples were stained for 3-5 days with alcian-alizarin staining solution made by adding 1 volume each of 0.3% alcian blue (Sigma) in 70% ethanol, 0.1% alizarin red (Sigma) in 95% ethanol and glacial acetic acid to 17 volumes of 70% ethanol. After staining, samples were rinsed twice with deionised water and destained with 1% KOH (in deionised water) till the soft tissue cleared and skeletal elements were visible (usually 1-4 days depending on the age of the sample). Samples were further destained in 20%, 50% and 80% glycerol diluted with 1%KOH until the desired staining contrast was achieved (approximately 1-2days for each dilution). Samples were stored and imaged in 100% glycerol at room temperature. Images were obtained on a Leica MZ16 stereomicroscope using a ringed bright light source.

Mice and rats

30-day-old C57BL/6 mice (body weight 14.59±0.72g) and 10-day-old Sprague Dawley rats (body weight 20±0.49g) were purchased from Charles River Laboratories and Janvier Labs (Europe). C57BL/6 mice used for the axitinib experiments were purchased from Charles River Laboratories. Col2-Cre:Sik3-FL/FL mice were obtained from Dr. Henry Kronenberg, Massachusetts General Hospital. The Sik3-FL/FL mice were originally purchased from EUCOMM and the Col2-Cre mice were obtained from Richard R. Behringer, University of Texas MD Anderson Cancer Center[47]. Prx-Cre:Gsα^{R201H} mice were generated by Dr. Murat Bastepe, Massachusetts General Hospital and was described previously[33].

Dissection and culturing of the tibia and femur

From both hind legs of 30-day-old mice and 10-day-old rats, the tibia and femur bones were dissected out aseptically in DMEM/F12 medium supplemented with 50 µg/ml gentamycin (dissection medium) on ice, with removal of as much surrounding tissue as possible. The height and diameters of the top and side surfaces of the epiphysis were measured with a digital caliper. For each animal, one set of tibia and femur was used for control and the other for treatment. All comparisons involved the bones from the same animal.

Still in dissection medium on ice, the bones were subjected to pressure with the Instron ElectroPuls E1000 Test Instrument. Load was applied at a speed of 0.1 N per second and load/digital position curves recorded in the Bluehill 3 software. Control bones went through the same procedures, but without loading.

For culturing, bones were first washed twice in dissection medium before being placed into DMEM/F12 medium supplemented with 1 mM β-glycerophosphate, 0.2% bovine serum albumin, 50 µg/ml ascorbic acid and 50 µg/ml gentamycin for 48 hours as described previously[25]. Propidium iodide (stock solution at 1 mg/ml, Sigma) was added to the culture medium at a ratio of 1:50 30 minutes before termination of culturing. The

tibia and femur were then fixed in 4% PFA overnight, decalcified, cleared in 30% sucrose overnight (at 4° C) and finally embedded in optimal cutting temperature (OCT) compound for frozen sectioning. When applying the load, the medial tibia plateau flanked by the tibia bone grooves is always facing one direction and the angled pressure was applied always to one side of the plateau (on top of one of the grooves). When embedding in OCT for sectioning, the bone is always placed into the grid with the medial tibia plateau facing upward and sectioned frontally to ensure the pressure direction during imaging.

Calculation of mechanical and material properties

Determination of the position of the bone relative to the position of its fixture yielded the deformation value. Stiffness was defined as the slope of the initial linear portion of the load-deformation curve. Stress was calculated by distributing the load equally over the top (vertical load) or side surface (angular load) of the epiphysis, assuming that both of these surfaces were oval. Strain was calculated by distributing the bone deformation equally along the height of the epiphysis. The initial linear portion of the stress-strain curve up to 0.2% offset was plotted together with the stress-strain curve itself in the same graph and the intersection of the line and curve defined as the 0.2% offset yield strength.

Axitinib Injection

Axitinib (Sigma) was dissolved in DMSO and injected intraperitoneally at a dose of 0.25mg per animal per day for the C57BL/6 mice for 8 (P21 to P27) or 10 days (P18 to P27 or P21 to P30) Control group of the C57BL/6 mice receive the same volume of DMSO injection each day. Transgenic Prx-Cre:Gsα^{R201H} mice and corresponding Gsα^{R201H} controls were injected daily 0.017 mg per gram of body weight between postnatal 21 and 29 days of age to block elimination of dead hypertrophic chondrocytes by ingrowing blood vessels. Animals were sacrificed one day after the last axitinib injection.

TUNEL staining

30-µm thick sections of cultured tibia bones were treated with proteinase K (Ambion) at 10 µg/ml for 40 minutes at 37° C before applying the TUNEL reaction mix (Roche Inc.) for 90 minutes. The cells were then counter-stained with DAPI for 30 minutes.

Quantification of positive cells (PI+, TUNEL+, YAP+ etc)

For each data point of the PI+ and TUNEL+ cell number quantification, at least three sections per animal and at least three animals were analyzed. Double blind counting was performed for all quantification analysis, including the medio-lateral distribution of PI+, TUNEL+, Caspase-3+, p73+, YAP+ and double p73+YAP+ cells.

Immunofluorescent staining

30-µm sections of cultured tibia bones were blocked in 3% normal horse serum for one hour, followed by overnight incubation with primary antibodies against cleaved caspase

3 (1:500) (Cell Signaling), YAP (1:50) (Santa Cruz), p73 (1:100) (Abcam) or Ki67 (1:20) (Invitrogen) at 4° C. Secondary antibodies tagged with fluorophore were then added for one hour followed by DAPI counter-staining for 30 minutes.

In situ hybridization

In situ hybridization was performed on 30-µm sections as described previously[48] utilizing a probe against ColXa1 (a gift from Prof. Bjorn Olsen, Harvard Medical School) labelled with digoxigenin (DIG) in accordance with the manufacturer's instructions (Roche Inc.). Samples were then treated with either DIG antibody Fab fragments (Sigma) and NTM (Sigma) for colorimetric visualization or DIG antibody HRP (Sigma) and TSA kit (Perkin Elmer) for fluorescent visualization.

Atomic Force Microscopy

120-150-µm thick sections of live rat tibia bones were obtained by vibratome (Thermo Fisher Scientific) and mounted onto glass discs using silicone grease from the Bruker fluid cell accessory kit (Bruker, USA). The force spectroscopy measurements were performed using a MultiMode 8 atomic force microscope with a Nanoscope V controller and E scanner (Bruker). The regions of cells of interest for the acquisition of force-distance curves were selected under the optical microscope in combination with the AFM instrument.

The force-distance curves were acquired employing CP-PNP-BSG colloidal probes (NanoandMore GmbH, Germany) with a 5-µm borosilicate glass microsphere attached to the 200-µm cantilever. The spring constants of the cantilevers (measured by the thermal tune procedure) were 0.06-0.09 N/m.

All measurements were conducted at 25^0 C and all tissue was handled in DMEM/F12 HEPES-containing medium on ice. At least 70 individual force-distance curves were acquired for each type of cell by ramping over the surface and totally 30 cells were measured from 3 different animals. These force-distance curves were processed with the NanoScope Analysis v.1.10 software (Bruker). Utilizing retract curves, the elastic modulus E was extracted from these force-distance curves by fitting in accordance with the Hertzian model of contact mechanics.

Nanoindentation

Local mechanical characteristics of 10-day-old rat and 30-day-old mice cartilage samples were measured with a Piuma Nanoindenter (Optics11, Netherlands) adapted for soft materials. Measurements were performed on 220-250-µm sections of alive tissues (without fixation and freezing) obtained by vibratome (Thermo Fisher Scientific) at 2-4°C. After the measurement, the sections were stained with PI (Sigma) and CalceinAM (Sigma) to confirm cell viability.

Nanoindenter includes a controller, an optical fiber and a spherical tip for the force-displacement curves acquisition. The tip is attached to a flexible cantilever, the displacement of which after the contact with a surface is measured using an interferometer via an optical fiber.

To measure the Young's modulus the probe was immersed for 5 μm into the sample at each point of measurement. The Young's modulus for each point was computed according to the Hertzian contact mechanics model for a spherical body indenting a flat surface, using the built-in Piuma software.

For the study of 10-day-old rat and 30-day-old mice cartilage mechanical characteristics, we used a cantilever with the spring constant of 4.14 N/m and a tip with the 45.5 μm radius of curvature. The measurements were conducted in Phosphate buffered saline (PBS) cooled to 2-4°C to maintain cell viability. The samples were immobilized with specially designed holder immersed in cold PBS. During the measurements the probe was always located inside the fluid medium at a sufficient depth, in order to avoid measurement errors due to adhesion forces at the air-water boundary. The area of the Young's modulus mapping for rat samples was 1350×400 μm with the step of 45 μm by the X-axis and 100 μm by the Y-axis. For mice the area of mapping was 585×360 μm with the step of 45 μm by the X- and Y-axes. Based on the results of the measurements, the effective Young's modulus was computed, its distribution over the surface was plotted and mean ± standard deviation (SD) Young's modulus value calculated.

Finite Element Analysis

The effects of an SOC on the distribution of stress in the zones of bone growth were explored by numerical simulations. Following the reasoning of [27], a plane-strain 2D domain was considered, to simplify the complex geometry of the bone end, and thereby clarify fundamental aspects of the response. The model thus took five sub-domains into consideration. The geometry of this simulation domain was a slight modification of [27], with a total height of 66 mm, radius at the top of 17 mm, and bottom width of 25 mm. The cortical bone was given a width of 2.5 mm (measured horizontally). The thickness normal to the 2D plane was by definition 1 mm. Only the top part of the model is shown in results figures.

The main parameter in these simulations was the presence or absence of an SOC or other stiffer tissues, introduced by providing this domain with a stiffness at least equal to that of the cartilage domain. Non-linear strains were taken into consideration, but the materials in all subdomains were considered to be linearly elastic, as described by a Young's modulus E_i and a Poisson ratio ν_i. We used the same material properties as [27], and in particular for cartilage E_C= 6 MPa, ν_C= 0.47. When included, the SOC was defined in a subdomain with E_D= 500 MPa, ν_D= 0.20. Thus, the stiff tissue had the material properties of dense cancellous bone, i.e., approximately 80-fold stiffness compared to cartilage.

In all cases, the bottom edge of the complete model had zero displacement vertically, and the outside edges of the cortical bone zero displacement horizontally. Applied to different 45° sectors of the semi-circular top, the pressure was modelled as maximal on the center of the given sector (300 kPa for physiological level, 3MPa for supra-physiological), falling quadratically and symmetrically to zero on the two neighboring sector borders. In light of the symmetry of the domain, only the top or right-hand side

was loaded (except for a verification case to [27], not shown). The direction and integrated total force of loading were affected slightly by the finite deformation of the domain.
Different components or comparison values of stress (measured as the second Piola-Kirchhoff stress relative to the unstressed reference volume) were evaluated. Primary focus was on the hydrostatic stress, the lowest principal stress (always compressive), and the octahedral shear stress, providing different perspectives on the response to external loading. Since the situations considered were dominated by compressive stresses, the signs for the two first have been changed in figures. Stress values are plotted on the deformed shape of the domain, without magnification of the deformation.
Numerical simulations of the response to loading were based on parameterized finite element approximations, and performed in the Comsol Multiphysics software (version 5.2, Comsol AB, Stockholm, Sweden.)
With similar loads, this model resulted in a stress distribution in and deformation of the cartilaginous epiphysis closely similar to those reported by [27].
Model design for stem tetrapods and archosaurs were based on [2,3] and [10,11] respectively.

Quantitative PCR

Proximal end growth plate of mouse and rat tibia was dissected and homogenized in liquid nitrogen for subsequent RNA extraction by Trizol and RNA purification by the RNeasy kit (Qiagen). Only RNA samples with an A260/A280 value between 1.8 and 2.0 were used. Extracted RNA was reverse transcribed into cDNA using a kit from Takara. qPCR was performed using the SYBR Green I supermix (BioRad) and analyzed using the ΔCt method by normalizing with the house keeping gene GAPDH. Three growth plates from independent animals were analyzed for each condition.

Statistical analysis

The values presented as means ± standard deviations of at least three independent experiments. The unpaired Student's t-test and one way ANOVA were utilized to calculate P-values if not otherwise indicated.

Figures

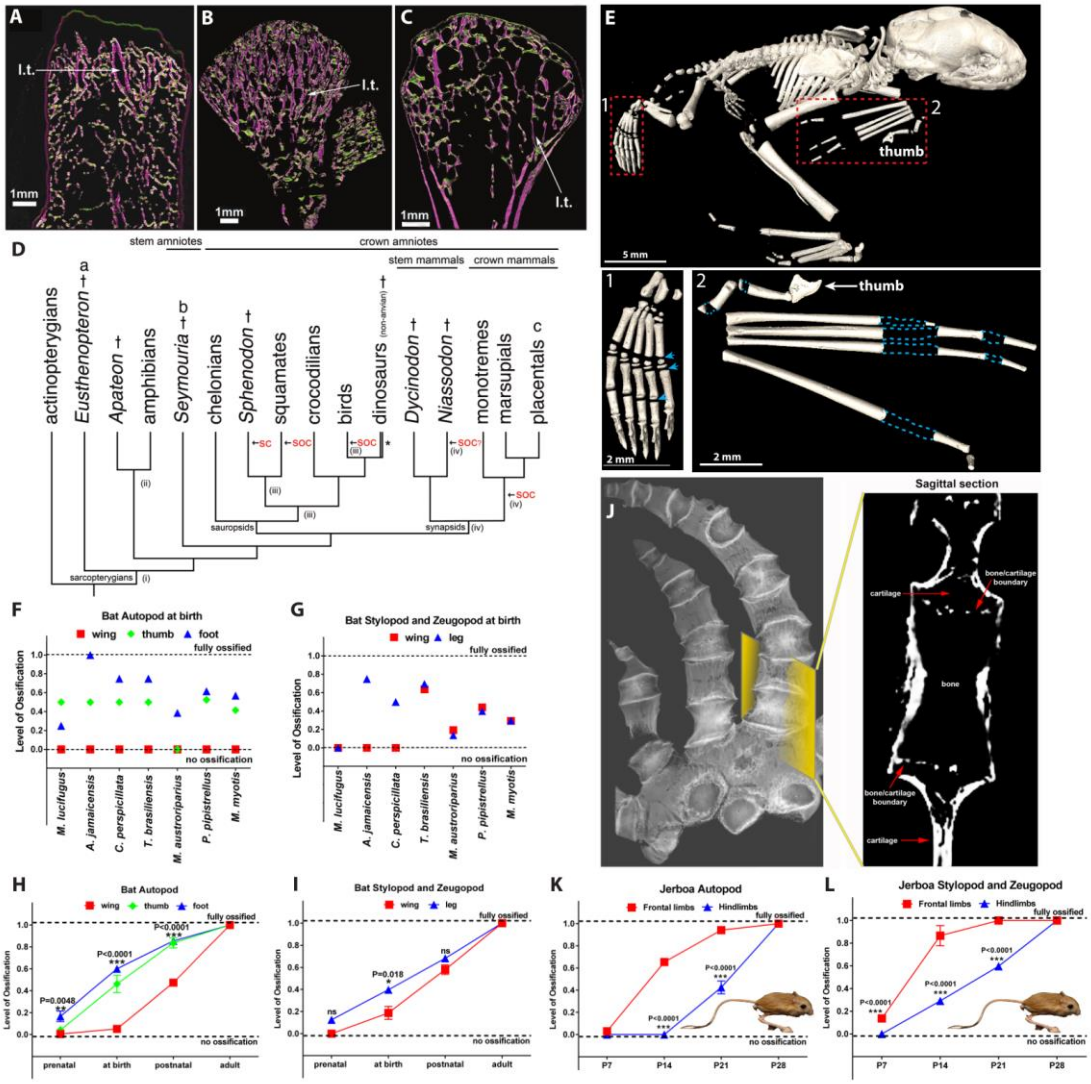

Fig. 1 Evolutionary appearance of the SOC and its correlation with the mechanical demands.

(**A** to **C**) The proximal humeral metaphyses of Eusthenopteron (A), Seymouria (B) and Sciurus vulgaris (red squirrel) (C). The longitudinal trabeculae resulting from endochondral ossification at the base of the growth plate in adults are shown in pink, while the transverse trabeculae appear green. The longitudinal trabeculae (l.t.) are designated marrow processes invading the growth plate. (**D**) Phylogeny of osteichthyans, illustrating the major changes in the evolution of long-bone epiphyses. The black arrows indicate the presence of a secondary center (SC) or a secondary ossification center (SOC). (i) Estimated appearance of endochondral formation of long bones, based on the fossil record to date; (ii) Cartilaginous epiphyses in long-bones; (iii) Hypothetical presence of an ancestral SCs in sauropsids; (iv) Hypothetical presence of an ancestral SOCs in synapsids. * indicates paraphyly within the group. (**E**) microCT image of a 1-3-days-old bat Pipistrellus pipistrellus. (1) foot, with arrows pointing to growth plates, (2) wing, with dashed blue lines outlining the areas of non-ossified cartilage. (**F** and **G**) Ossification of the autopod (F) and of the stylopod and zeugopod (G) in 7 bat species at birth. (**H** and **I**) Generalized pattern of ossification of the autopod (H) and stylopod and zeugopod (I) of 6 bat species combined (Myotis lucifugus, Artibeus jamaicensis, Carollia perspicillata, Tadarida

brasiliensis, Myotis austroriparius and Myotis myotis). (**J**) CT image of an adult killer whale Orcinus orca and a virtual sagittal section of the metacarpal II demonstrating the absence of the SOC. (**K** and **L**) Ossification of the autopod (K) and stylopod and zeugopod (L) of *Jaculus jaculus* (three-toed jerboa) at various postnatal stages. Data are means ± SD representing inter-individual variation, One-way ANOVA. In (K) and (L), n=2 jerboa analyzed. ns, not significant.

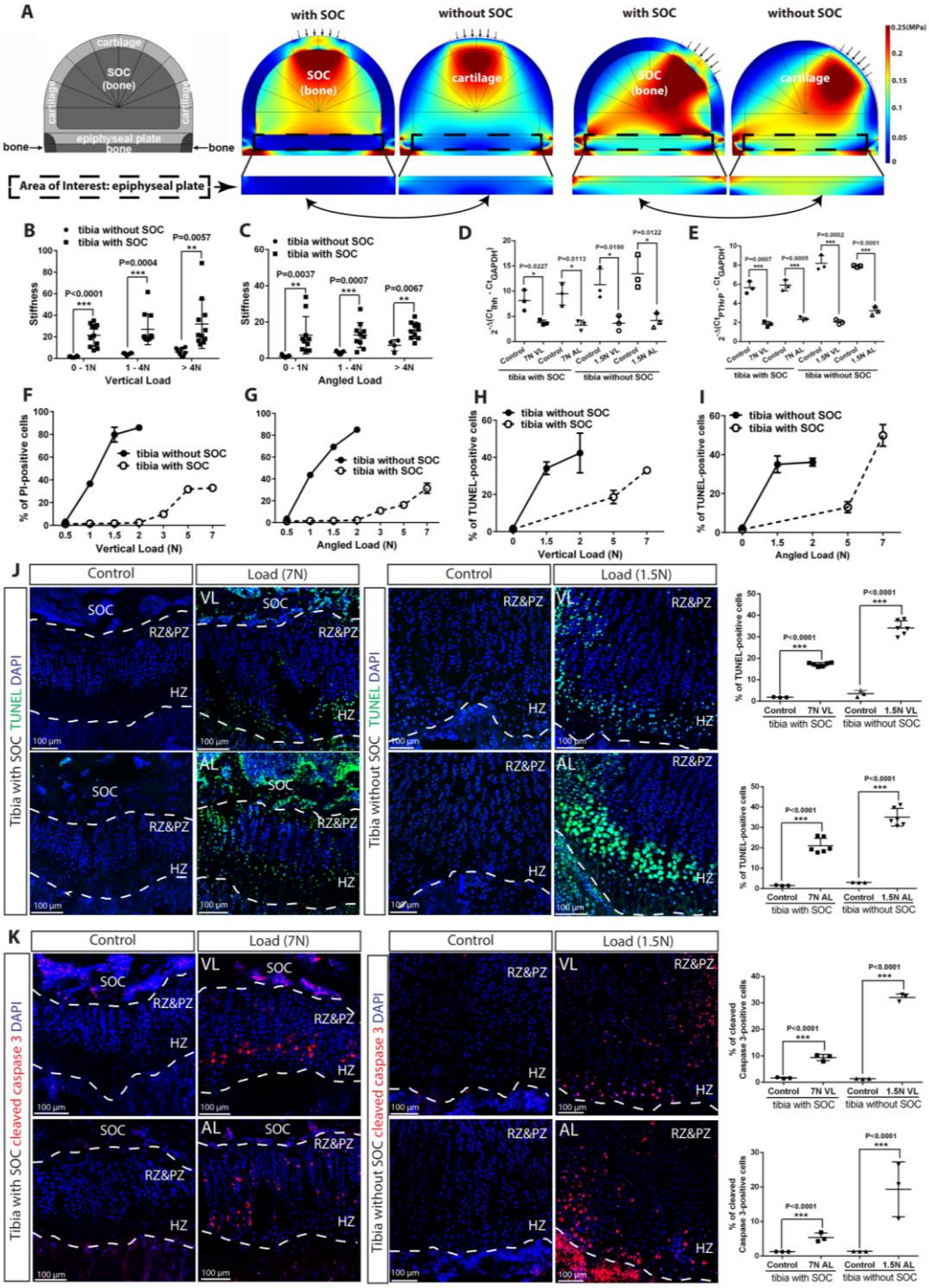

Fig. 2 The SOC protects epiphyseal chondrocytes from apoptosis induced by mechanical stress.

(**A**) Octahedral stress from FEA modeling with physiological loading level. The small arrows indicate the direction of loading. The two-headed curved arrows indicate areas for comparison. (**B** and **C**) The stiffness of bones with fully developed SOCs (tibia with SOC) and with immature SOCs (tibia without SOC) was measured at different loads and in both the vertical (B) and angled (C) direction. (**D** and **E**) QPCR analysis of Indian hedgehog (Ihh) (D) and parathyroid hormone related peptide (PTHrP) (E) levels in the epiphyseal end of tibia with and without SOCs. (**F** to **I**) Quantification of propidium iodide- (PI) (F and G) and TUNEL- (H and

I) positive cells in the growth plates of tibia with and without SOCs loaded vertically (F, H) or at an angle (G, I). (**J** and **K**) Representative images and quantification of TUNEL staining (green) (J) and cleaved Caspase 3 staining (red) (K) in the growth plates of loaded tibias with and without SOCs. DAPI was used for counterstaining (blue). Data are means ± SD, two-tailed Student's t test. In (B), n=10 for "tibia with SOC" at all loads; n=9 for "tibia without SOC" at 0–1N and 1-4N, n=4 for >4N. In (C), n=11 for "tibia with SOC" at all loads; n=8 for "tibia without SOC" at all loads. In (D) to (K), n=3. The control and loaded tibia were from the same animal. VL, vertical load, AL, angled load. RZ&PZ, resting zone & proliferative zone combined, HZ, hypertrophic zone. "tibia with SOC" and "tibia without SOC" in the figure refer to tibias from 30-day-old mice and 10-day-old rats respectively (see Fig. S5, B, C).

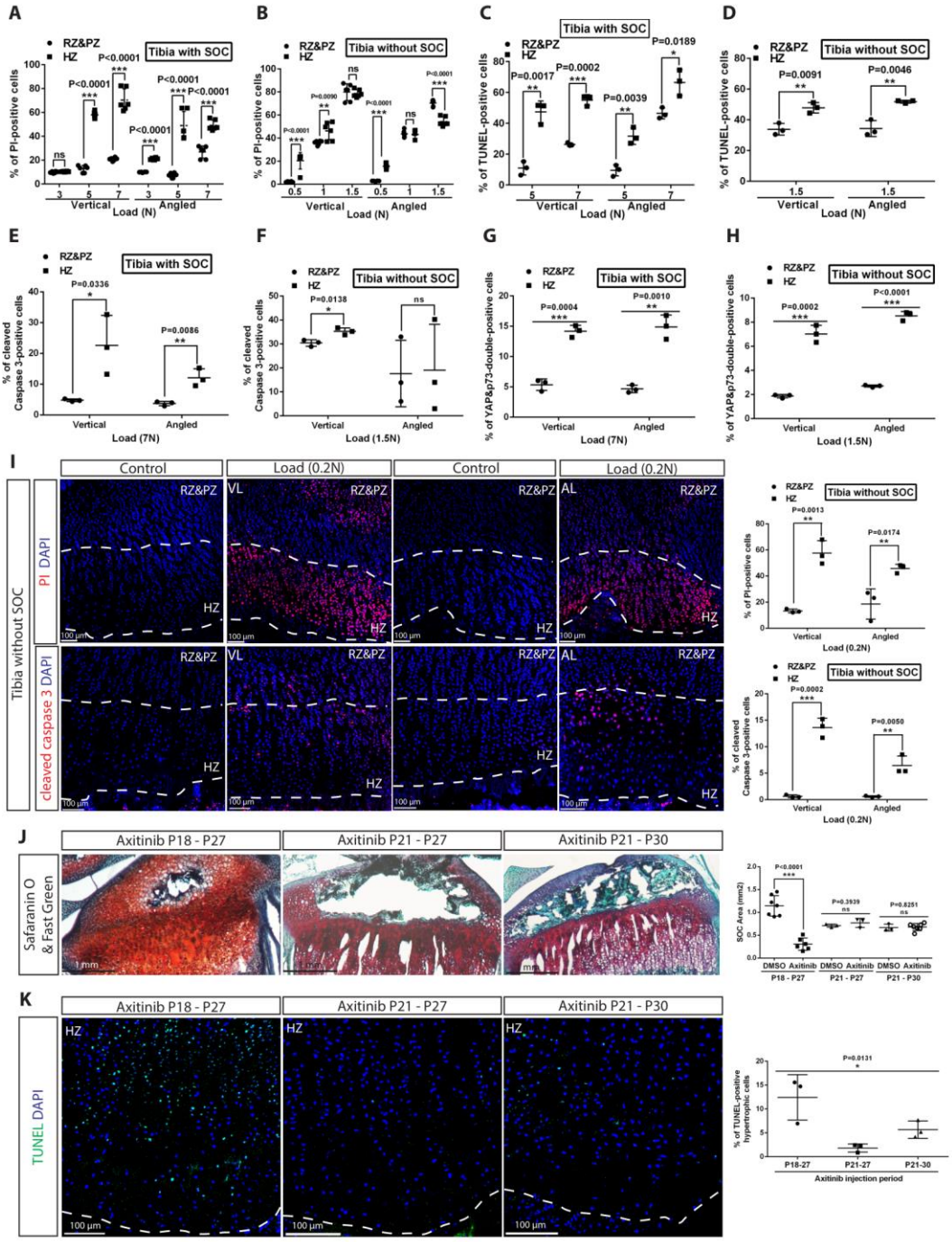

Fig. 3 Hypertrophic cells are the most sensitive cell type in response to mechanical stress. (**A** to **D**) Comparison of the extent of cell death between resting+proliferative zones (RZ&PZ) and hypertrophic zone (HZ) of the vertically and angularly loaded growth plates with (A and C) and without (B and D) SOCs as assessed by PI staining (A and B) and TUNEL (C and D). (**E** to **H**) Distribution of immunohistological staining along longitudinal axis for cleaved Caspase-3 staining (E to F) and YAP&p73 double staining (G to H) of the vertically and angularly loaded tibia with (E and G) and without (F and H) SOCs. (**I**) Representative images and quantification of propidium iodide (PI) staining (upper panel) and cleaved Caspase 3 staining (lower panel) in the growth plates of vertically or angularly 0.2N loaded tibias without SOCs. The control and loaded tibia were from the same animal. (**J**) Representative histology images of the tibia epiphysis and quantification of the SOC size of wild type mice injected with

Axitinib at various time periods. P refers to postnatal day. (**K**) Representative images and quantification of TUNEL staining (green) in the hypertrophic cells of the tibia growth plate of the Axitinib injected mice. DAPI was used for counterstaining (blue) in I and K. Data are means ± SD, two-tailed Student's t test. In (A) to (K), n=3. ns, not significant. "tibia with SOC" and "tibia without SOC" refer to tibias from 30-day-old mice and 10-day-old rats respectively (see Fig. S5, B, C).

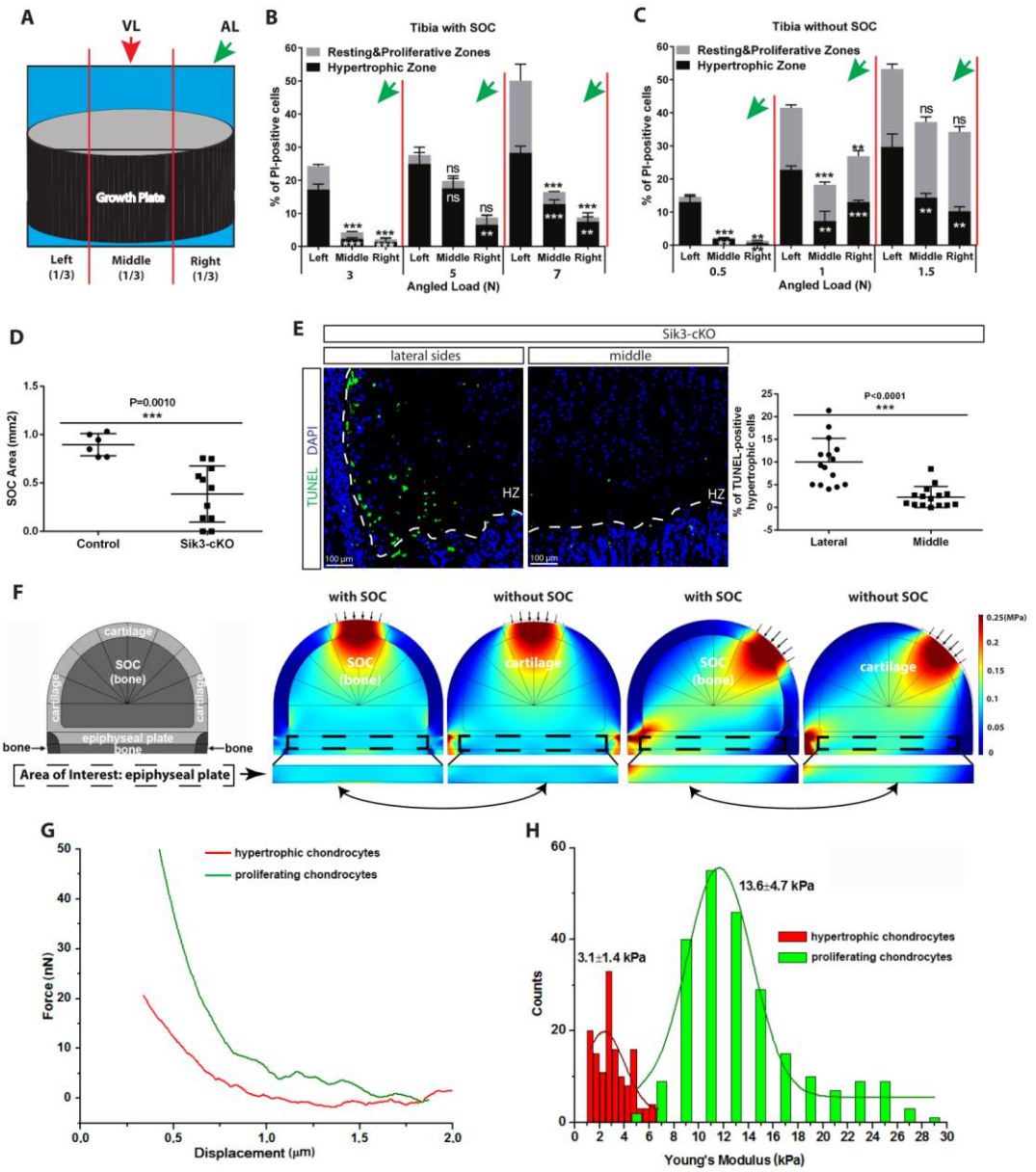

Fig. 4 Low stiffness of hypertrophic chondrocytes renders them sensitive to mechanical stress.

(**A**) Schematic illustration of a section plan and loading directions in relation to the quantitative analysis of cell death distribution in the lateral-medial direction presented in (B and C). The growth plate is divided into three equal parts, (left, middle and right) in relationship to the angle at which the load is applied (green or red arrows). (**B** and **C**) Quantification of propidium iodide (PI)-positive chondrocytes in the resting&proliferative zones and hypertrophic zone of tibias with (B) and without (C) SOCs subjected to an angled load (AL, green arrow, always applied from the right). Data are means ± SD, One-way ANOVA. **, P<0.001 and ***, P<0.0001 in comparison with the left portion. ns, not significant. The black and white asterisks indicate the significance for the resting&proliferative and hypertrophic zones, respectively. (**D**) Quantification of the SOC size of postnatal day 28 Sik3-FL/FL (Control) and Col2-Cre:Sik3-FL/FL (Sik3-cKO) mice. (**E**) Representative images and quantification of TUNEL staining (green) between the lateral and middle parts of Sik3-cKO mice. DAPI was used for counterstaining (blue). HZ, hypertrophic zone. In (D) and (E), data are means ± SD, two-tailed

Student's t test, n=3 for "Control" and n=5 for "Sik3-cKO". (**F**) Principal compressive stress from FEA modeling with physiological loading level. The small arrows indicate the direction of loading. The two-headed curved arrows indicate areas for comparison. (**G**) Typical force curves for hypertrophic and proliferating chondrocytes obtained by atomic force microscopy. (H) Comparison of the elastic moduli of hypertrophic and proliferating chondrocytes.

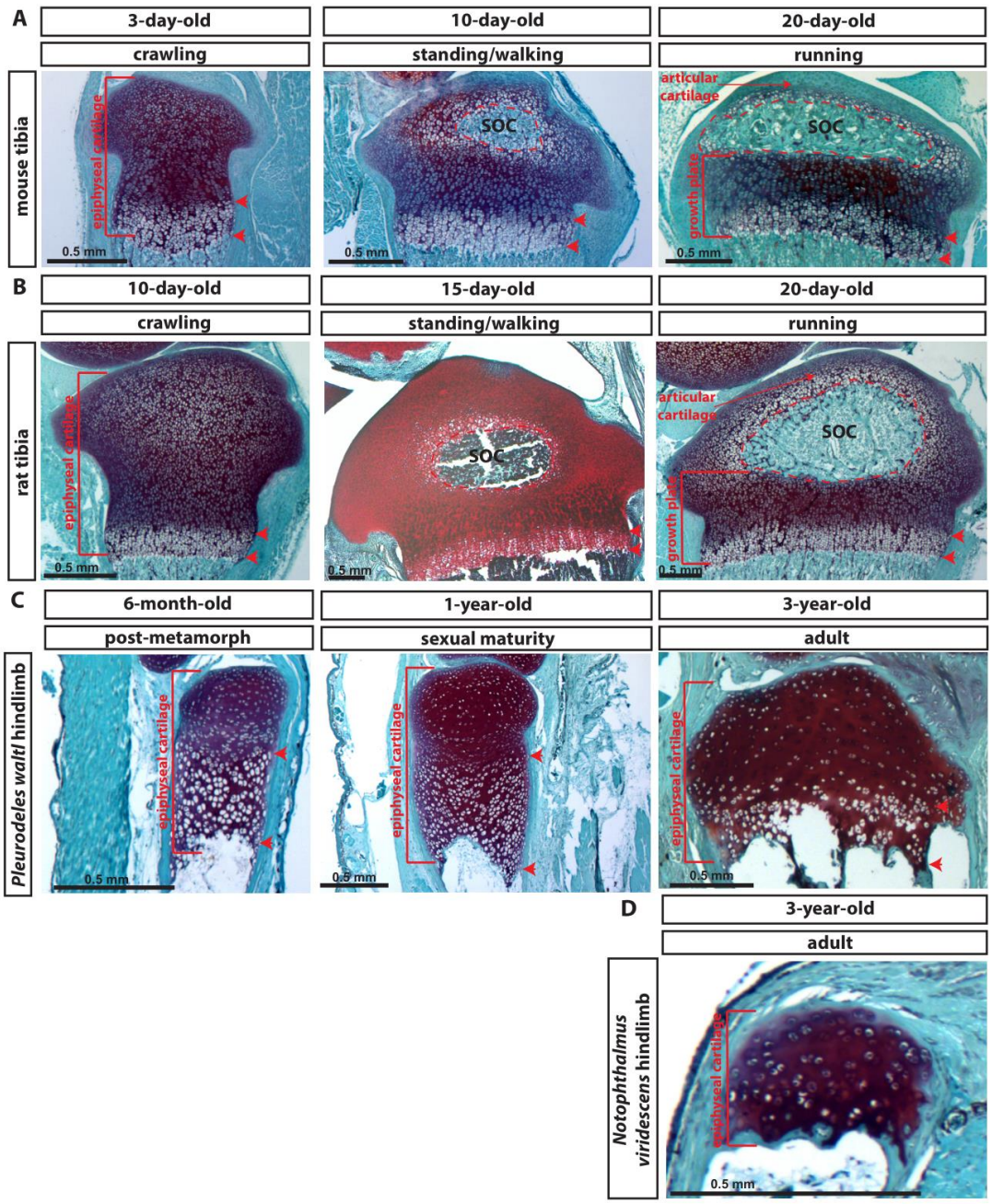

Fig. S1 Development of articular and epiphyseal cartilage in rodents and salamanders.

(**A** to **D**) Representative safranin O and fast green staining of sections of the epiphyseal end of the tibia of mouse (A), rat (B), and the hind limb of salamander species Pleurodeles waltl (C) and Notophthalmus viridescens (D). The dashed red lines outline the SOC. Red arrow heads mark the zone of hypertrophic cells. Walking behavior is indicated according to our daily observations. Pleurodeles waltl is a Spanish newt that spends most their life in water. Notophthalmus viridescens is an American newt that has an aquatic juvenile stage and a terrestrial adult stage.

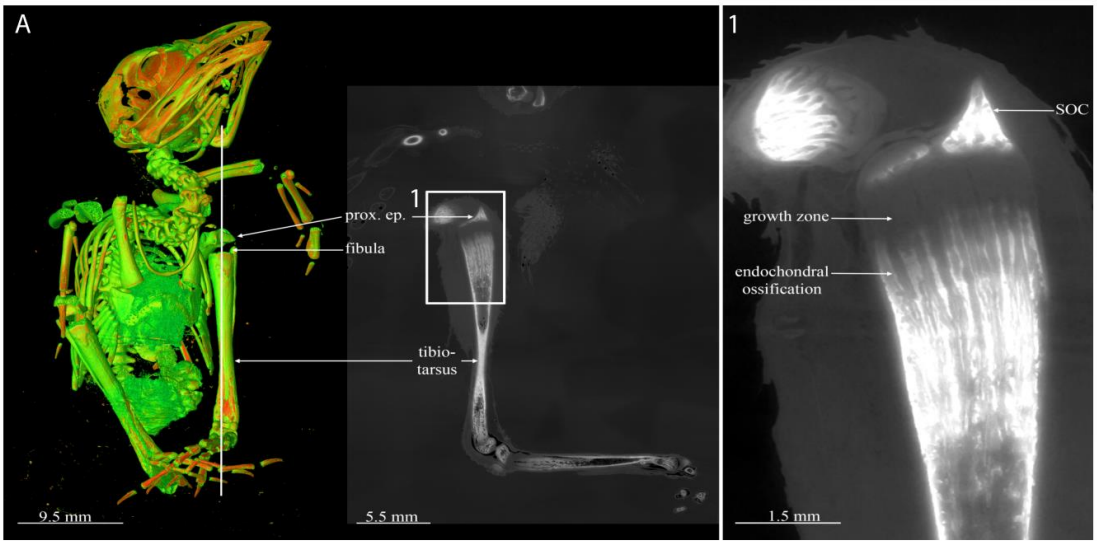

Fig. S2 (A) A synchrotron scan of a juvenile sparrow demonstrates the presence of SOC. 1, a virtual thin section of the proximal epiphysis. prox. ep., proximal epiphysis.

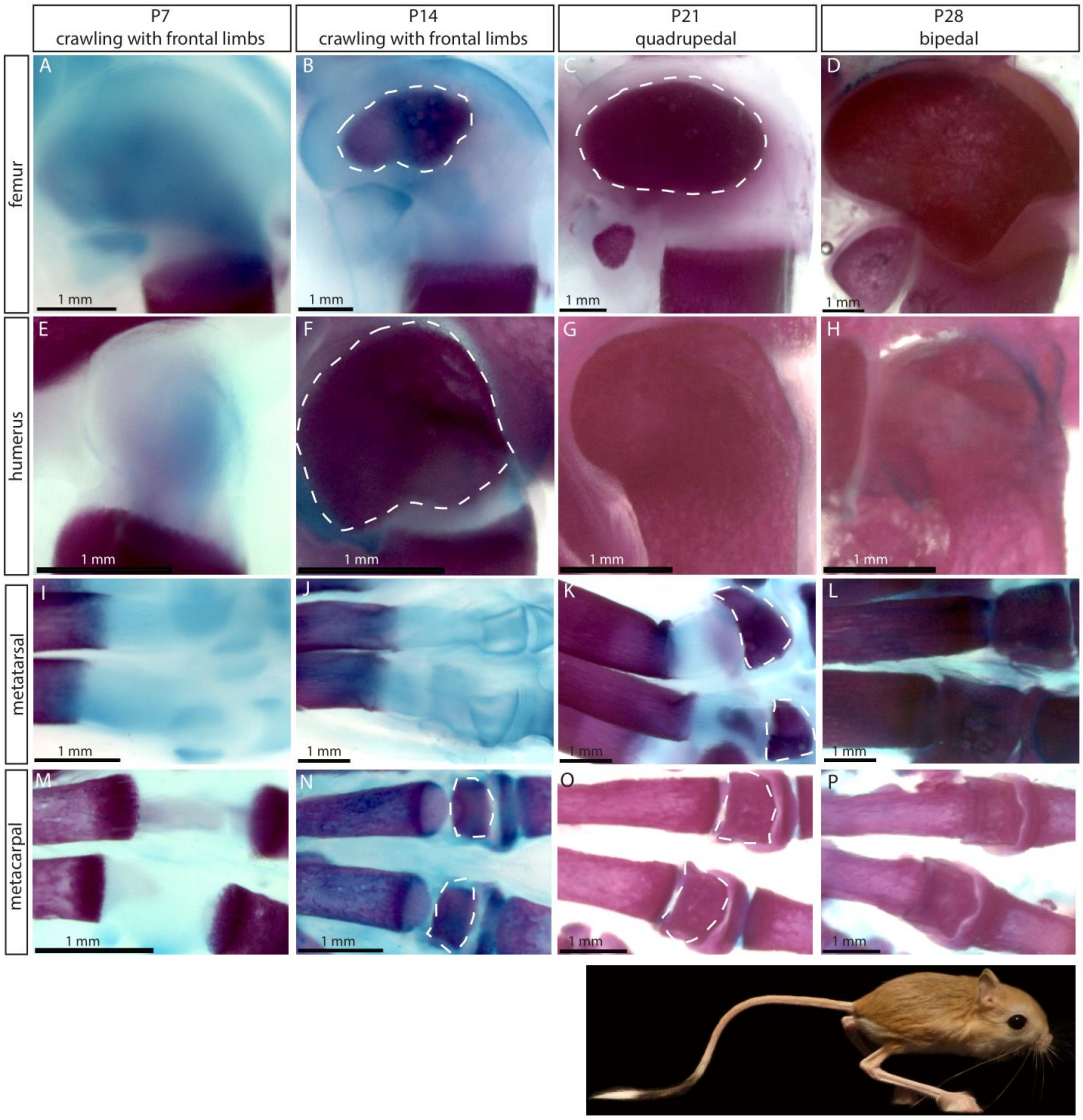

Fig. S3 (**A** to **P**) Alcian blue and alizarin red staining of femur (A to D), humerus (E to H), metatarsal (I to L) and metacarpal (M to P) of *Jaculus jaculus* (three-toed jerboa) at various postnatal (P) time points. The dashed white lines outline the SOC. The gait pattern was derived from our weekly observations (see Video S2).

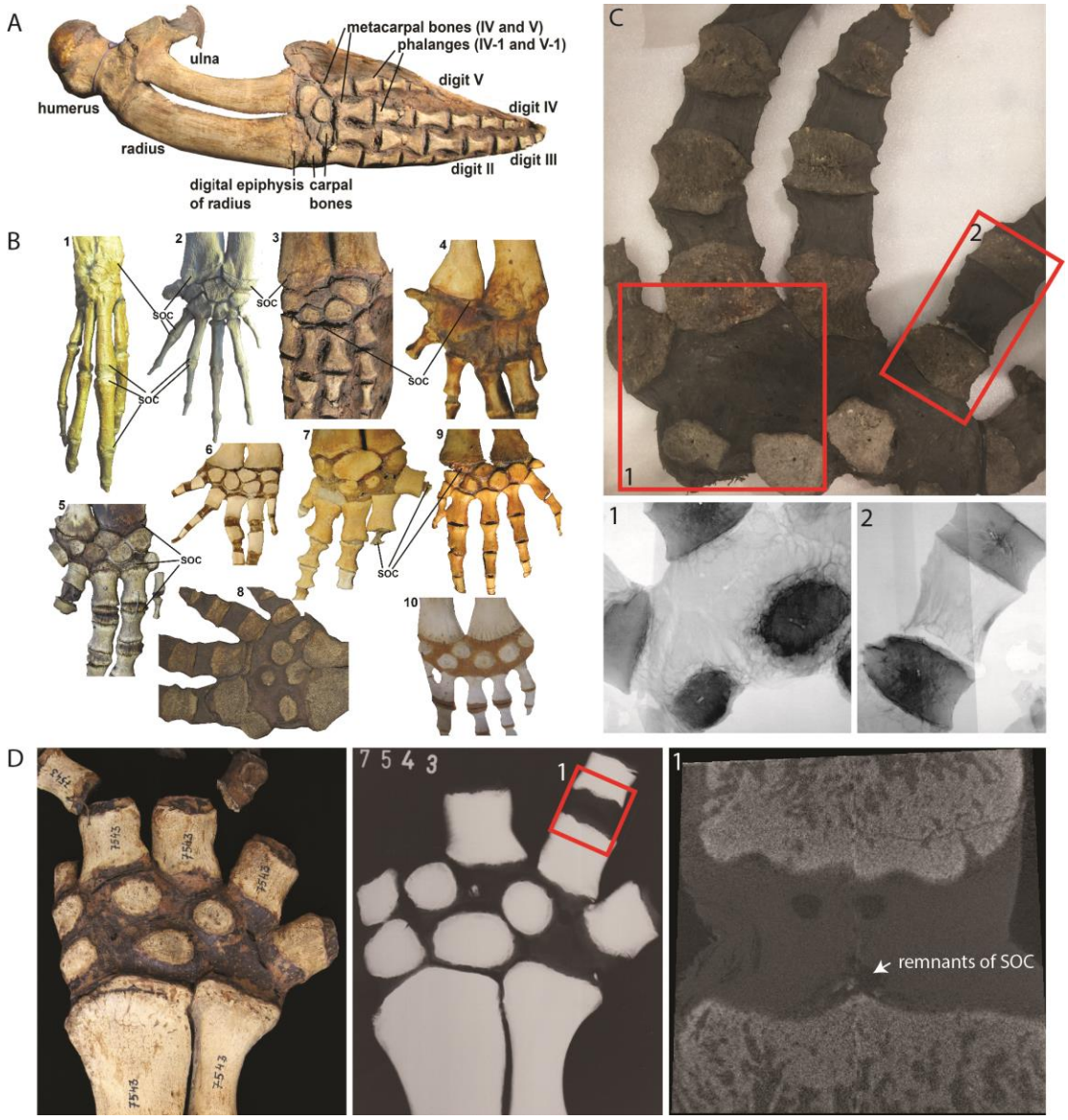

Fig. S4 (**A**) Forelimb bones of the minke whale Balaenoptera acutorostrata. (**B**) Comparative anatomy of bony and cartilaginous epiphyses in the distal portion of the forelimbs of various cetacean whales. (B1) *Maiacetus inuus*, (B2) *Dorudon atrox*, (B3) minke whale *Balaenoptera acutorostrata*, (B4) North Atlantic right whale *Eubalaena glacialis*, (B5) pilot whale *Globicephala melas*, (B6) boto river dolphin *Inia geoffrensis*, (B7) narwhal *Monodon monoceros*, (B8) killer whale *Orcinus orca*, (B9) juvenile and (B10) subadult sperm whale *Physeter catodon*. (**C**) Sample image of an adult killer whale *Orcinus orca* (same species as B8) with X-ray images of the highlighted areas (1, 2) from the corresponding image on their left. (**D**) Sample (left) and X-ray (right) images of an adult beluga whale *Delphinapterus leucas*. (D1) Micro-CT reconstruction of the highlighted phalange joint.

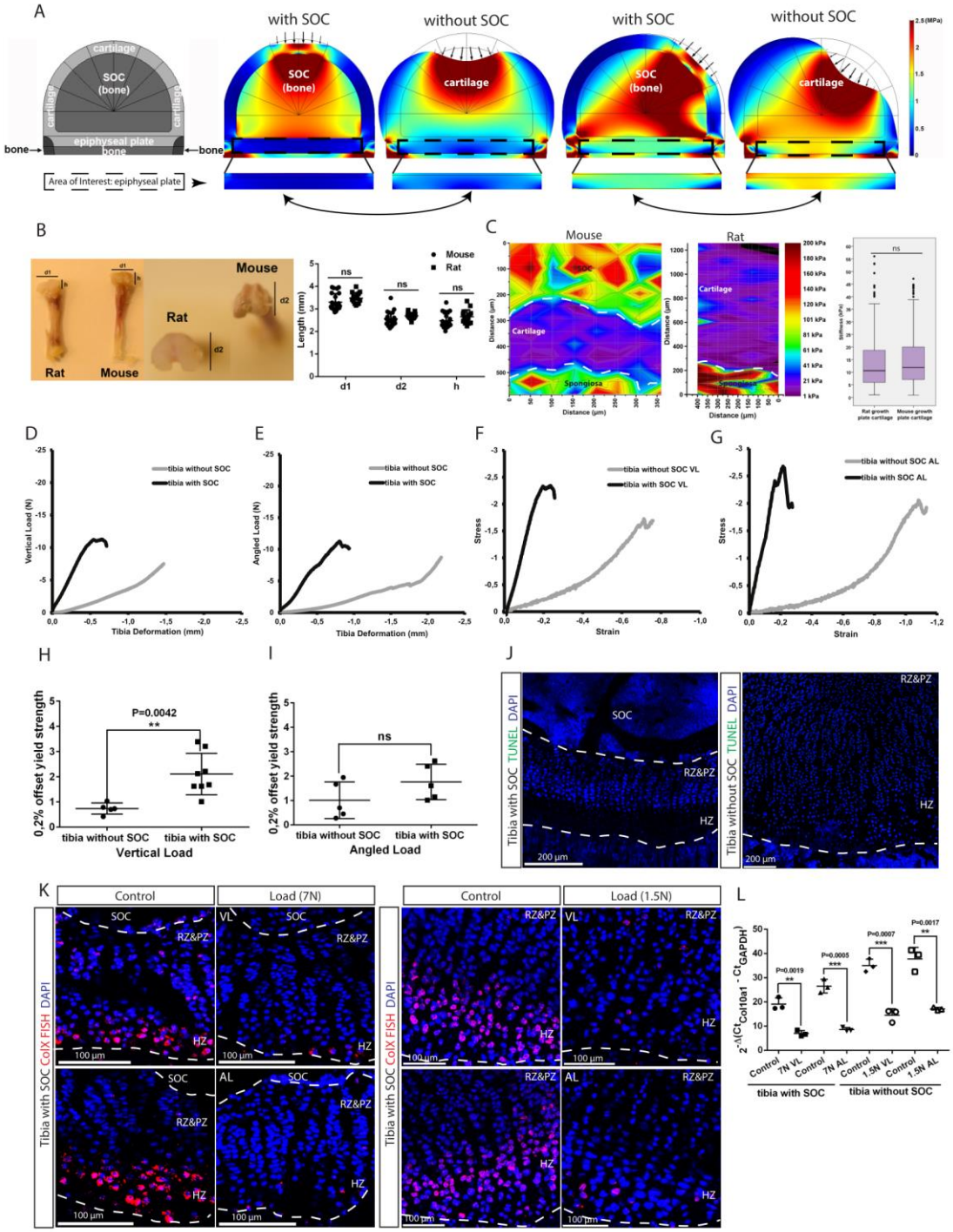

Fig. S5 (**A**) Octahedral stresses from FEA modeling with supra-physiological loading level (3 MPa). The small arrows indicate the direction of loading and the two-headed curved arrows indicate areas for comparison. (**B**) Mouse (30-day-old) and rat (10-day-old) tibia with and without an SOC, respectively, have similar physical dimensions of the epiphyseal part (d1, d2, h). (**C**) Representative images and quantification of the nanoindentation test of 30-day old mice and 10-day-old rats. (**D** to **G**) Representative load/deformation (D and E) and stress/strain (F and G) curves of vertically (VL) (D and F) and angularly (AL) (E and G) loaded tibias with and without SOCs. (**H** and **I**) Elasticity of tibias with and without SOCs under vertical (H) and angled load (I). (**J**) Representative images of growth plates of tibias with and without SOCs fixed after

dissection and prior loading. TUNEL staining (green) and nucleus counterstaining with DAPI (blue). (**K**) Fluorescent in situ hybridization of Collagen type X (ColX) in the loaded growth plates of tibias with and without SOCs. VL, vertical load, AL, angled load. RZ&PZ, resting zone & proliferative zones, HZ, hypertrophic zone. (**L**) QPCR analysis of ColX level in the epiphyseal end of tibia with and without SOCs exposed to different loading. Data are means ± SD, two-tailed Student's t test, except in (C) where Mann-Whitney U test was used. In (B), n=23 for "Mouse" and n=15 for "Rat". In (C), n=5 for "Mouse" and n=4 for "Rat". In (H), (I) and (L), n=3. ns, not significant.

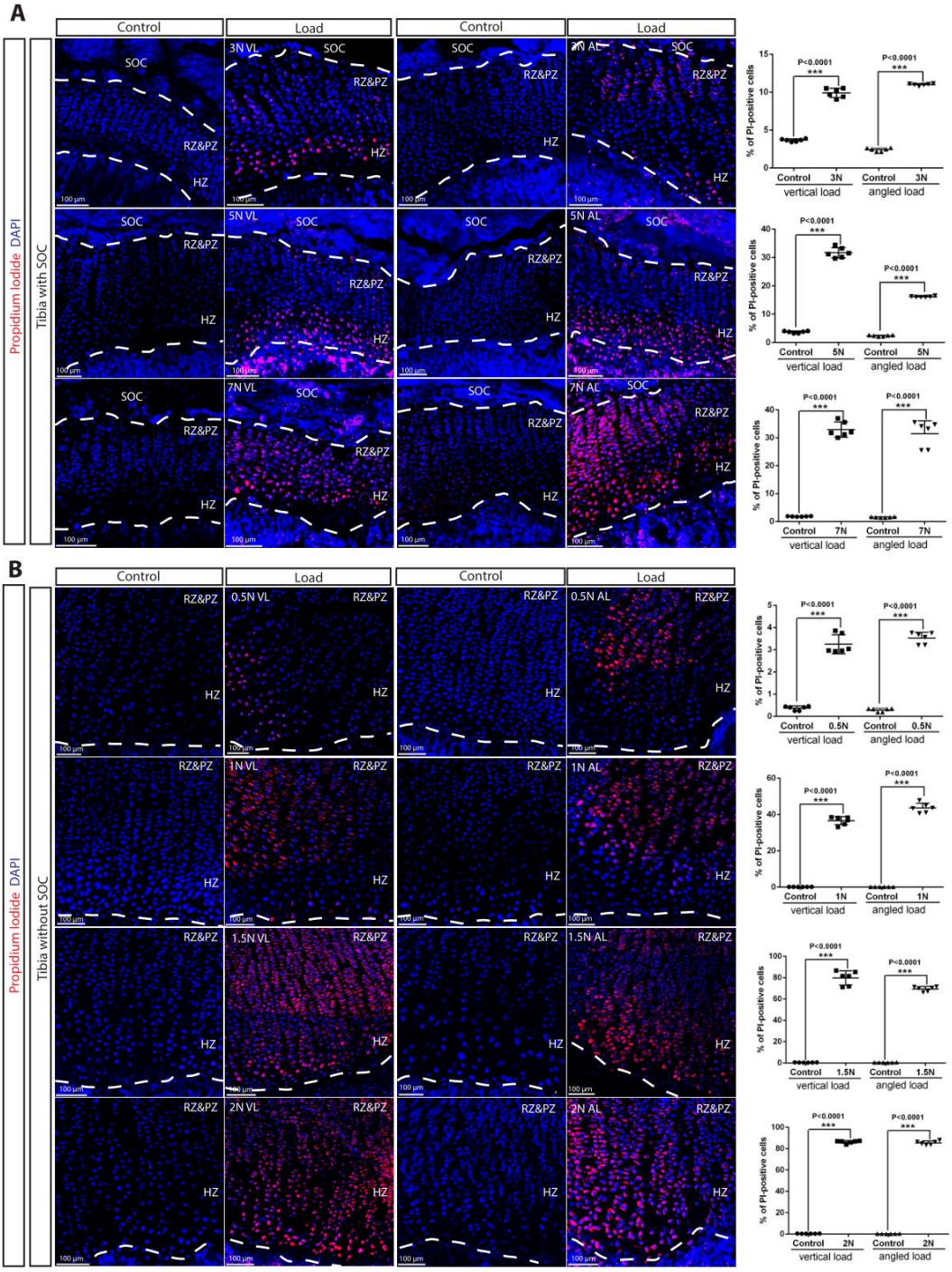

Fig. S6 (**A** and **B**) Representative images and quantification of the distribution of propidium iodide (PI)-positive cells in the growth plates of tibia with (A) and without a SOC (B) loaded vertically or angularly. RZ&PZ, resting zone & proliferative zones, HZ, hypertrophic zone. "tibia with SOC" and "tibia without SOC" refer to tibias from 30-day-old mice and 10-day-old rats respectively (see Fig. S5, B, C). Data are means ± SD, two-tailed Student's t test. In (A) and (B), n=3.

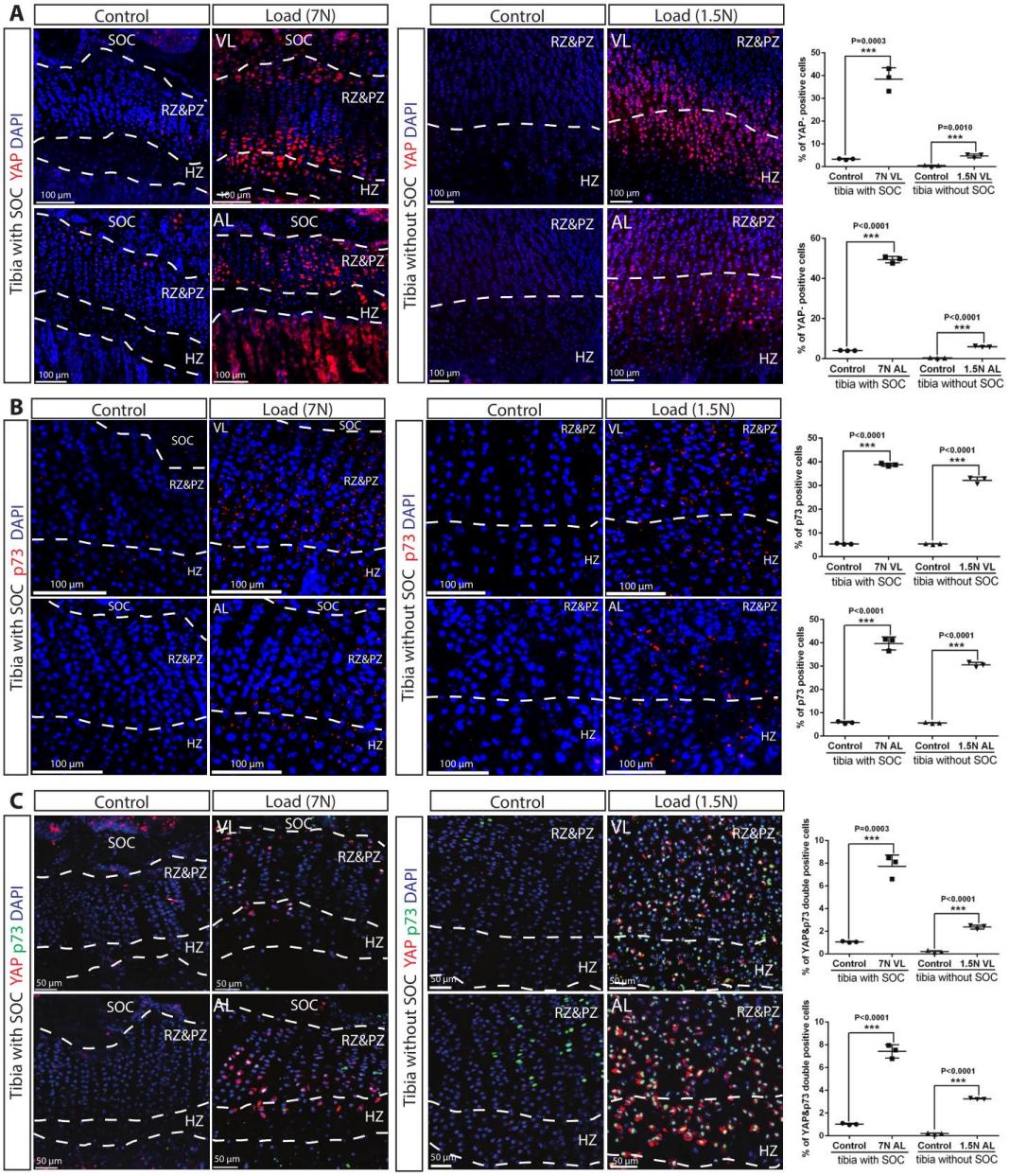

Fig. S7 (**A** to **C**) Immunostaining and quantification of YAP (A), p73 (B) and YAP + p73 double positive cells (C) in the growth plates of loaded tibias with and without SOCs loaded vertically (VL) and angularly (AL). RZ&HZ, resting zone & proliferative zone, HZ, hypertrophic zone. "tibia with SOC" and "tibia without SOC" refer to tibias from 30-day-old mice and 10-day-old rats respectively (see Fig. S5, B, C). Data are means ± SD, two-tailed Student's t test. In (A) to (C), n=3.

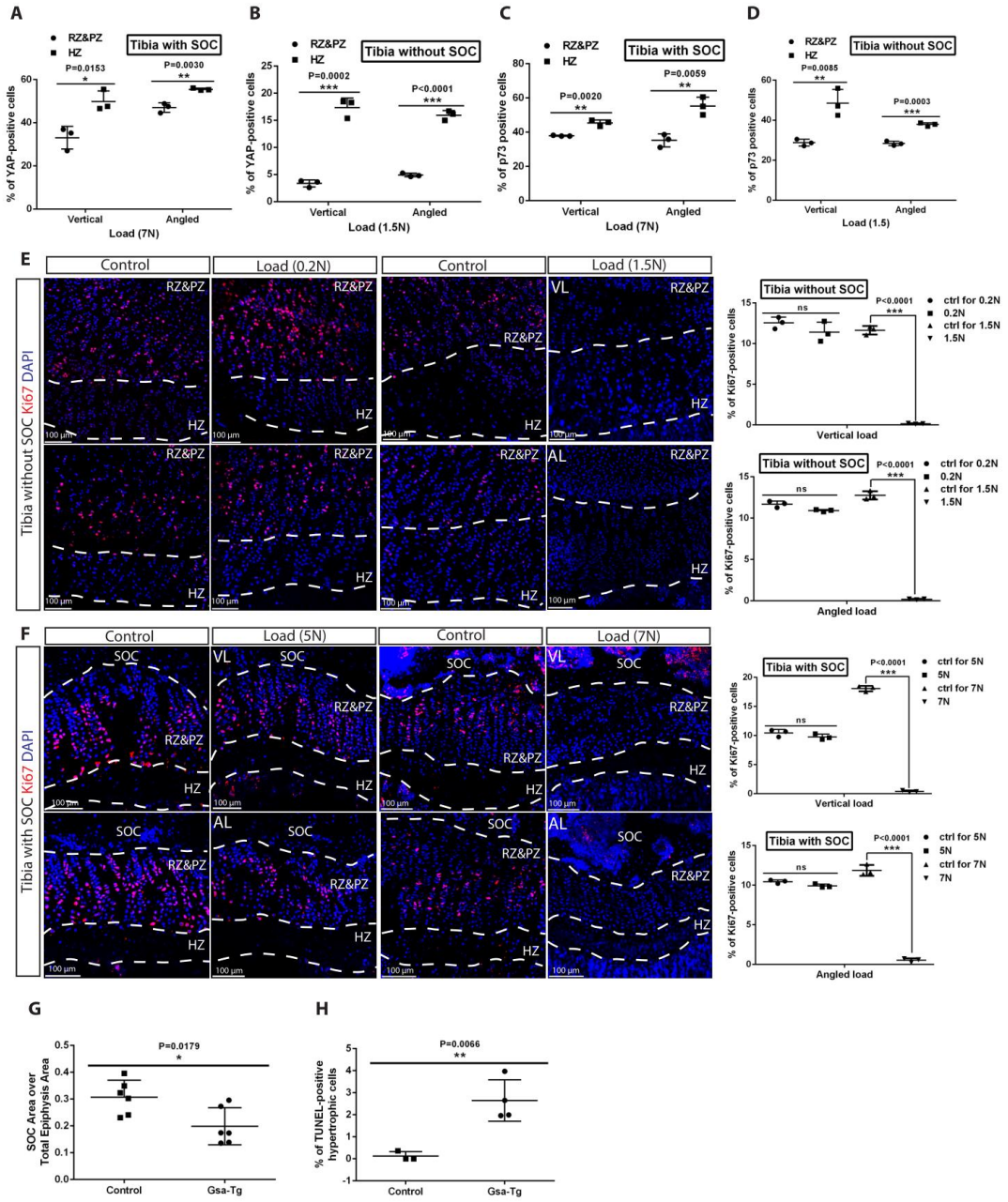

Fig. S8 (**A** to **D**) Comparison of YAP (A and B) and p73 (C and D) staining between the resting plus proliferative zones (RZ&PZ) and hypertrophic zone (HZ) in the growth plates of tibias with (A and C) and without (B and D) SOCs. (**E** and **F**) Representative images and quantification of the ki67 staining in the growth plates of tibias with (F) and without (E) SOCs. (**G** and **H**) Quantification of SOC size (G) and TUNEL staining (H) of the hypertrophic cells in the growth plates of $_{stop}Gs\alpha^{R201H}$ (Control) and Prx-Cre:$Gs\alpha^{R201H}$ (Gsα-Tg) mice. Data are means ± SD, two-tailed Student's t test. In (A) to (H), n=3. ns, not significant.

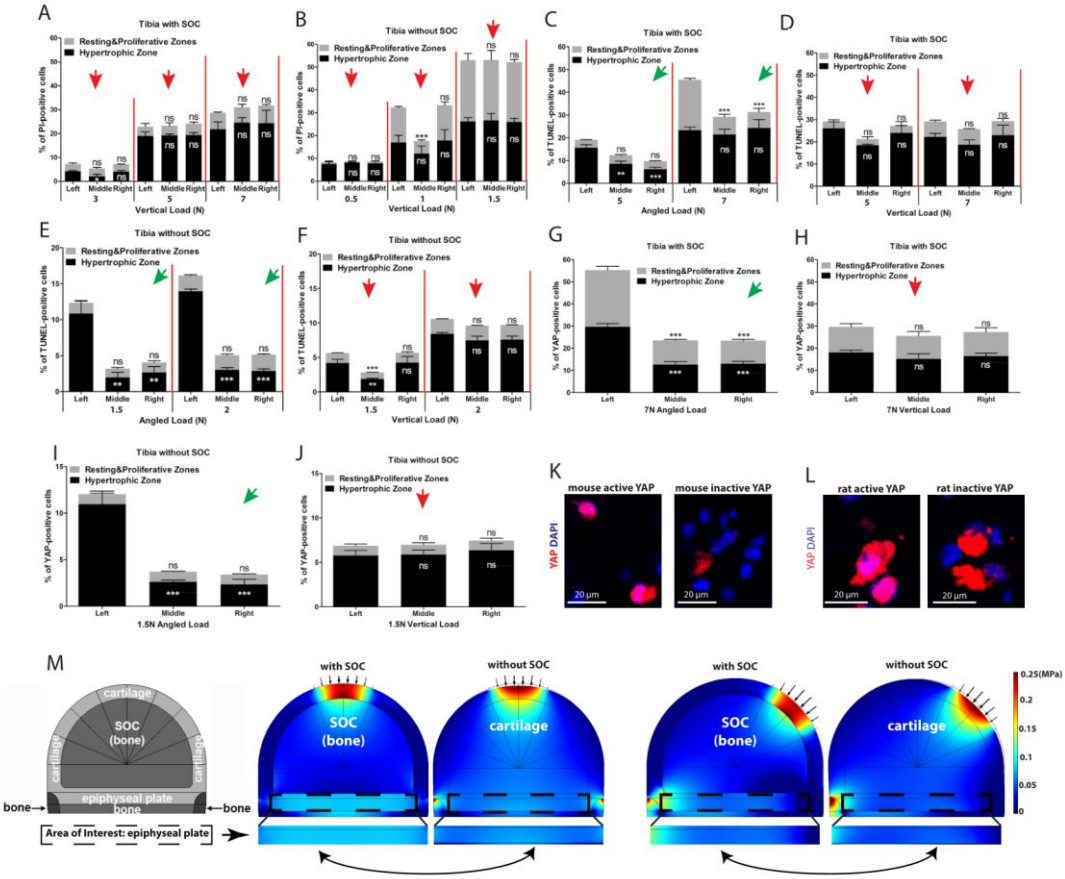

Fig. S9 (**A** and **B**) Quantification of PI-positive chondrocytes in relation to lateral-medial direction of the growth plate of tibia loaded vertically with (A) and without (B) an SOC (see Fig. 4A for details). (**C** to **F**) Quantification of TUNEL-positive chondrocytes in relation to lateral-medial direction of the growth plate of tibia with (C and D) and without (E and F) an SOC subjected to angular (C, E) and vertical (D, F) loading. (**G** to **J**) Quantification of distribution of YAP-positive chondrocytes in relation to lateral-medial direction within the resting&proliferative and hypertrophic zones of the growth plate of angularly (G, I) and vertically (H, J) loaded tibia with (G and H) and without (I and J) an SOC. Only nuclearized active YAP as demonstrated in k-l was quantified. The red and green arrows indicate the direction of loading (see the legend to Fig. 4a for more details). Data are means ± SD, One-way ANOVA. **, P<0.001 and ***, P<0.0001. In (A) to (J), n=3. ns, not significant.The black and white asterisks indicate p-values for the resting&proliferative and hypertrophic zones, respectively. (**K** and **L**) Immunostaining of active (nuclear) and inactive YAP in mouse (K) and rat (L) chondrocytes. (**M**) Hydrostatic compressive stress on epiphyseal plates from FEA modelling with physiological loading level. The small arrows indicate the direction of loading and the two-headed curved arrows indicate areas for comparison.

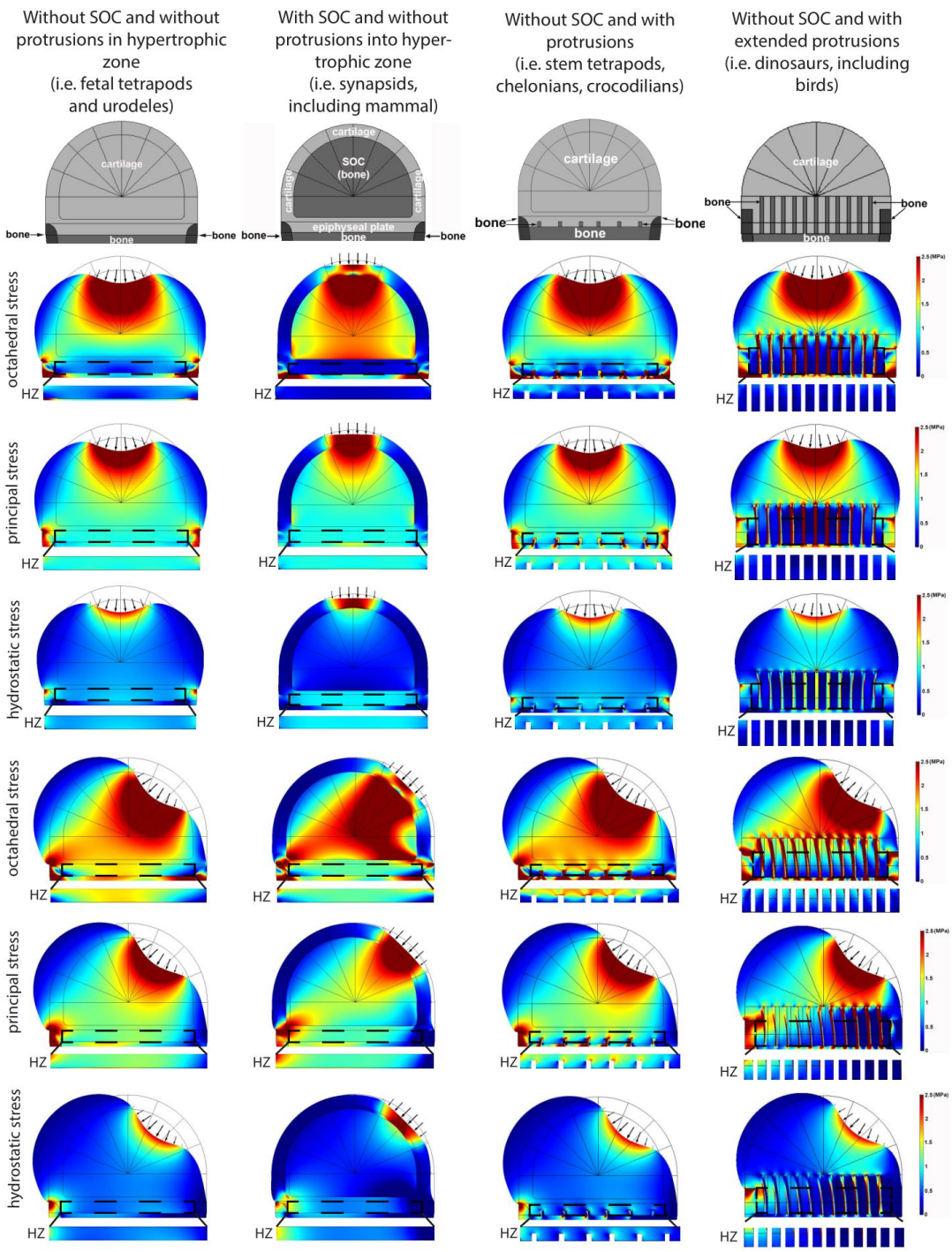

Fig. S10 Deformation and distribution of comparison stresses from FEA simulation in different evolutionary taxa. Columns refer to (from left to right) "without SOC" (representing i.e., fetal tetrapods and urodeles), "with SOC" (representing i.e., synapsids including mammal), "stem tetrapods" (representing i.e., juvenile stem tetrapods, chelonians, crocodilians) and archosaurs (representing i.e., birds and non-avian dinosaurs). For comparison of structural functionality, all situations used the same basic geometry and materials. The small arrows indicate the direction of loading. Supra-physiological loading level (3 MPa) was modeled. The illustrations of octahedral stress on without SOC and with SOC are identical to those in Fig. S2, A and are

presented here to allow direct comparison. Hypertrophic zone free of bony elements is presented under each model for direct comparison. Hypertrophic zone, HZ.

Video S1 3D model based on microCT surface images of a 1-3-day-old Pipistrellus pipistrellus s.l. (common pipistrelle bat). The age could not be determined more precisely.

Video S2 CT scan of the manus of a killer whale Orcinus orca.

Video S3 Development of a gait pattern of Jerboa.

Supplementary data file S1 Primary data on the level of ossification of the individual bones of all species of Chiroptera analyzed.

Author Contributions

A.S.C. designed the study. M.X. conceived the study under the guidance of A.S.C. M.X. performed all of the experiments except those specified below. P.G. performed the studies on SOC evolution in cetaceans. K. G. helped with X-ray scans with the Beluga whale. A.N.H., B.M., K.F. and I.A. analyzed SOC development in chiroptera. J.E., P.T. and S.S. modeled the synchrotron scan data and examined SOC evolution in early tetrapods, amphibians and stem amniotes. L.L., P.N. and M.C. assisted with the biological experiments. M.K. and A.S. assisted with the experiments on rat and salamander, respectively. I.L.A. and C.G. helped with application of the load testing instrument. P.T., E.V.M., S.K., B.S. and A.A. performed the atomic force microscopy and nanonindentation analysis. L.T.S. and M.B. performed experiments on Prx-Cre:Gsα^{R201H} mice. S.N. and H.M.K. contributed to experiments with SIK3 cKO mice. A.S. and K.C. contributed jerboa experimental data. A.E. developed the finite element analysis. M.X. and A.S.C. wrote the paper with the help of I.A, S.S. P.G and A.N.H. All authors critically reviewed this manuscript and approved the final draft.

References

1 Yang, L., Tsang, K. Y., Tang, H. C., Chan, D. & Cheah, K. S. Hypertrophic chondrocytes can become osteoblasts and osteocytes in endochondral bone formation. *Proceedings of the National Academy of Sciences of the United States of America* **111**, 12097-12102, doi:10.1073/pnas.1302703111 (2014).

2 Sanchez, S., Tafforeau, P. & Ahlberg, P. E. The humerus of Eusthenopteron: a puzzling organization presaging the establishment of tetrapod limb bone marrow. *Proc Biol Sci* **281**, 20140299, doi:10.1098/rspb.2014.0299 (2014).

3 Sanchez, S., Tafforeau, P., Clack, J. A. & Ahlberg, P. E. Life history of the stem tetrapod Acanthostega revealed by synchrotron microtomography. *Nature* **537**, 408-411, doi:10.1038/nature19354 (2016).

4 Hall, B. K. *Bones and Cartilage Developmental and Evolutionary Skeletal Biology*. 2 edn, (Elsevier Academic Press, 2005).

5 Frobisch, N. B. & Shubin, N. H. Salamander limb development: integrating genes, morphology, and fossils. *Dev Dyn* **240**, 1087-1099, doi:10.1002/dvdy.22629 (2011).
6 Haines, R. W. The Primitive Form of Epiphysis in the Long Bones of Tetrapods. *J Anat* **72**, 323-343 (1938).
7 Haines, J.-S. The evolution of epiphyses and of endochondral bone. *Biological Review* **174**, 267-292 (1942).
8 Carter, D. R. & Wong, M. The role of mechanical loading histories in the development of diarthrodial joints. *J Orthop Res* **6**, 804-816, doi:10.1002/jor.1100060604 (1988).
9 Castanhinha, R. *et al.* Bringing dicynodonts back to life: paleobiology and anatomy of a new emydopoid genus from the Upper Permian of Mozambique. *PLoS One* **8**, e80974, doi:10.1371/journal.pone.0080974 (2013).
10 Chinsamy, A. & Abdala, F. Palaeobiological implications of the bone microstructure of South American traversodontids (Therapsida : Cynodontia). *S Afr J Sci* **104**, 225-230 (2008).
11 Ray, S. & Chinsamy, A. Diictodon feliceps (Therapsida, Dicynodontia): Bone histology, growth, and biomechanics. *J Vertebr Paleontol* **24**, 180-194, doi:Doi 10.1671/1914-14 (2004).
12 Horner, J. R., Padian, K. & Ricqlès, A. d. . Comparative osteohistology of some embryonic and perinatal archosaurs: developmental and behavioral implications for dinosaurs. *Paleobiology* **27**, 39-58 (2001).
13 Hughes, P. M., Rayner, J. M. V., Jones, G. . Ontogeny of 'true'flight and other aspects of growth in the bat Pipistrellus pipistrellus. *Journal of Zoology* **236**, 291-318 (1995).
14 Powers, L. V., Kandarian, S. C., Kunz, T. H. . Ontogeny of flight in the little brown bat, Myotis lucifugus: behavior, morphology, and muscle histochemistry. *Journal of Comparative Physiology A: Neuroethology, Sensory, Neural, and Behavioral Physiology* **168**, 675-685 (1991).
15 Elangovan, V., Yuvana Satya Priya, E., Raghuram, H. & Marimuthu, G. Wing morphology and flight development in the short-nosed fruit bat Cynopterus sphinx. *Zoology (Jena)* **110**, 189-196, doi:10.1016/j.zool.2007.02.001 (2007).
16 Wang, L., Lin, A., Xiao, Y., Jiang, T., Feng, J. Postnatal development in the big-footed bat, Myotis macrodactylus: wing morphology, echolocation calls, and flight. *Acta theriologica* **59**, 435-441 (2014).
17 Adams, R. A., Thibault, K. M. . Ontogeny and evolution of the hindlimb and calcar: assessing phylogenetic trends. *Ontogeny, functional ecology, and evolution of bats*, 316-332 (2000).
18 Hermanson, J. W. & Wilkins, K. T. Growth and development of two species of bats in a shared maternity roost. *Cells Tissues Organs* **187**, 24-34, doi:10.1159/000109961 (2008).
19 Koyabu, D. & Son, N. T. Patterns of postcranial ossification and sequence heterochrony in bats: life histories and developmental trade-offs. *J Exp Zool B Mol Dev Evol* **322**, 607-618, doi:10.1002/jez.b.22581 (2014).
20 Kunz, T. H., Hood, W. R. . Parental care and postnatal growth in the Chiroptera. *Reproductive biology of bats*, 415-468 (2000).

1017 21 Racey, P. A., Entwistle, A. C. . Life-history and reproductive strategies of
1018 bats. *Reproductive biology of bats*, 363-414 (2000).
1019 22 Eilam, D. & Shefer, G. The developmental order of bipedal locomotion in the
1020 jerboa (Jaculus orientalis): pivoting, creeping, quadrupedalism, and
1021 bipedalism. *Developmental psychobiology* **31**, 137-142 (1997).
1022 23 Gingerich, P. D. *et al.* New protocetid whale from the middle eocene of
1023 pakistan: birth on land, precocial development, and sexual dimorphism.
1024 *PLoS One* **4**, e4366, doi:10.1371/journal.pone.0004366 (2009).
1025 24 Uhen, M. Form, function, and anatomy of Dorudon atrox (Mammalia,
1026 Cetacea): an archaeocete from the middle to late Eocene of Egypt. *Papers*
1027 *on Paleontology* **34**, 1-222 (2004).
1028 25 Cooper, L. N. Forelimb anatomy. *Encyclopedia of marine mammals, 2nd*
1029 *edition*, 449-452 (2009).
1030 26 Mellor, L., Cooper, L. N., Torre, J., Brownell, Jr. R. L. . Paedomorphic
1031 ossification in porpoises with an emphasis on the vaquita (Phocoena
1032 sinus). *Aquatic Mammals* **35**, 193-202 (2009).
1033 27 Carter, D. R., MikiĆ, B., Padian, K. . Epigenetic mechanical factors in the
1034 evolution of long bone epiphyses. *Zoological Journal of the Linnean Society*
1035 **123**, 163-178 (1998).
1036 28 Chagin, A. S., Karimian, E., Sundstrom, K., Eriksson, E. & Savendahl, L. Catch-
1037 up growth after dexamethasone withdrawal occurs in cultured postnatal
1038 rat metatarsal bones. *J Endocrinol* **204**, 21-29, doi:10.1677/JOE-09-0307
1039 (2010).
1040 29 Dupont, S. *et al.* Role of YAP/TAZ in mechanotransduction. *Nature* **474**,
1041 179-183, doi:10.1038/nature10137 (2011).
1042 30 Strano, S. *et al.* Physical interaction with Yes-associated protein enhances
1043 p73 transcriptional activity. *J Biol Chem* **276**, 15164-15173,
1044 doi:10.1074/jbc.M010484200 (2001).
1045 31 Gerber, H. P. *et al.* VEGF couples hypertrophic cartilage remodeling,
1046 ossification and angiogenesis during endochondral bone formation. *Nat*
1047 *Med* **5**, 623-628, doi:10.1038/9467 (1999).
1048 32 Newton, P. T. *et al.* A radical switch in clonality reveals a stem cell niche in
1049 the epiphyseal growth plate. *Nature* **567**, 234-238, doi:10.1038/s41586-
1050 019-0989-6 (2019).
1051 33 Karaca, A. *et al.* Constitutive stimulatory G protein activity in limb
1052 mesenchyme impairs bone growth. *Bone* **110**, 230-237,
1053 doi:10.1016/j.bone.2018.02.016 (2018).
1054 34 Sasagawa, S. *et al.* SIK3 is essential for chondrocyte hypertrophy during
1055 skeletal development in mice. *Development* **139**, 1153-1163,
1056 doi:10.1242/dev.072652 (2012).
1057 35 Xu, X., Li, Z., Cai, L., Calve, S. & Neu, C. P. Mapping the Nonreciprocal
1058 Micromechanics of Individual Cells and the Surrounding Matrix Within
1059 Living Tissues. *Sci Rep* **6**, 24272, doi:10.1038/srep24272 (2016).
1060 36 Breur, G. J., Turgai, J., Vanenkevort, B. A., Farnum, C. E. & Wilsman, N. J.
1061 Stereological and serial section analysis of chondrocytic enlargement in the
1062 proximal tibial growth plate of the rat. *Anat Rec* **239**, 255-268,
1063 doi:10.1002/ar.1092390304 (1994).
1064 37 Wilsman, N. J., Farnum, C. E., Leiferman, E. M., Fry, M. & Barreto, C.
1065 Differential growth by growth plates as a function of multiple parameters

of chondrocytic kinetics. *J Orthop Res* **14**, 927-936, doi:10.1002/jor.1100140613 (1996).

38 Kozhemyakina, E., Lassar, A. B. & Zelzer, E. A pathway to bone: signaling molecules and transcription factors involved in chondrocyte development and maturation. *Development* **142**, 817-831, doi:10.1242/dev.105536 (2015).

39 Barreto, C., Albrecht, R. M., Bjorling, D. E., Horner, J. R. & Wilsman, N. J. Evidence of the growth plate and the growth of long bones in juvenile dinosaurs. *Science* **262**, 2020-2023, doi:10.1126/science.262.5142.2020 (1993).

40 Phillip T. Newton, L. L., Baoyi Zhou, Christoph Schweingruber, Maria Hovorakova, Meng Xie, Xiaoyan Sun, Lakshmi Sandhow, Artem V. Artemov, Evgeny Ivashkin, Simon Suter, Vyacheslav Dyachuk, Maha El Shahawy, Amel Gritli-Linde, Thibault Bouderlique, Julian Petersen, Annelie Mollbrink, Joakim Lundeberg, Grigori Enikolopov, Hong Qian, Kaj Fried, Maria Kasper, Eva Hedlund, Igor Adameyko, Lars Sävendahl, Andrei S Chagin. A radical switch in clonality reveals a stem cell niche in the epiphyseal growth plate. *Nature*, doi:https://doi.org/10.1038/s41586-019-0989-6 (2019).

41 Mehlman, C. T., Araghi, A. & Roy, D. R. Hyphenated history: the Hueter-Volkmann law. *Am J Orthop (Belle Mead NJ)* **26**, 798-800 (1997).

42 Sanchez, S., Ahlberg, P. E., Trinajstic, K. M., Mirone, A. & Tafforeau, P. Three-dimensional synchrotron virtual paleohistology: a new insight into the world of fossil bone microstructures. *Microscopy and microanalysis : the official journal of Microscopy Society of America, Microbeam Analysis Society, Microscopical Society of Canada* **18**, 1095-1105, doi:10.1017/S1431927612001079 (2012).

43 Paganin, D., Mayo, S. C., Gureyev, T. E., Miller, P. R. & Wilkins, S. W. Simultaneous phase and amplitude extraction from a single defocused image of a homogeneous object. *Journal of microscopy* **206**, 33-40 (2002).

44 Labiche, J. C. *et al.* Invited article: the fast readout low noise camera as a versatile x-ray detector for time resolved dispersive extended x-ray absorption fine structure and diffraction studies of dynamic problems in materials science, chemistry, and catalysis. *The Review of scientific instruments* **78**, 091301, doi:10.1063/1.2783112 (2007).

45 Jordan, B., Vercammen, P. & Cooper, K. L. Husbandry and breeding of the lesser Egyptian Jerboa, Jaculus jaculus. *Cold Spring Harb Protoc* **2011**, 1457-1461, doi:10.1101/pdb.prot066712 (2011).

46 Wallin, J. *et al.* The role of Pax-1 in axial skeleton development. *Development* **120**, 1109-1121 (1994).

47 Ovchinnikov, D. A., Deng, J. M., Ogunrinu, G. & Behringer, R. R. Col2a1-directed expression of Cre recombinase in differentiating chondrocytes in transgenic mice. *Genesis* **26**, 145-146 (2000).

48 Chagin, A. S. *et al.* G-protein stimulatory subunit alpha and Gq/11alpha G-proteins are both required to maintain quiescent stem-like chondrocytes. *Nat Commun* **5**, 3673, doi:10.1038/ncomms4673 (2014).